



Thermoelastic properties and γ' -solvus temperatures of single-crystal Ni-base superalloys

O. M. Horst^{1,*} , D. Schmitz² , J. Schreuer² , P. Git³ , H. Wang¹ , C. Körner³ , and G. Eggeler¹

¹Institut fuer Werkstoffe, Ruhr-Universitaet Bochum, Universitaetsstr. 150, 44801 Bochum, Germany

²Institut für Geologie, Mineralogie und Geophysik, Ruhr-Universitaet Bochum, 44801 Bochum, Germany

³Lehrstuhl WTM, Friedrich-Alexander-Universitaet Erlangen-Nuernberg, Martensstr. 5, 91058 Erlangen, Germany

Received: 9 September 2020

Accepted: 26 November 2020

Published online:

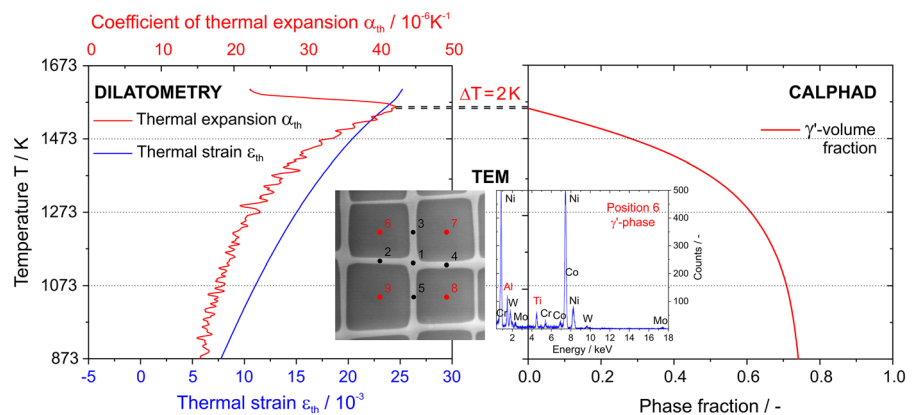
21 January 2021

© The Author(s) 2021

ABSTRACT

The present work shows that thermal expansion experiments can be used to measure the γ' -solvus temperatures of four Ni-base single-crystal superalloys (SX), one with Re and three Re-free variants. In the case of CMSX-4, experimental results are in good agreement with numerical thermodynamic results obtained using ThermoCalc. For three experimental Re-free alloys, the experimental and calculated results are close. Transmission electron microscopy shows that the chemical compositions of the γ - and the γ' -phases can be reasonably well predicted. We also use resonant ultrasound spectroscopy (RUS) to show how elastic coefficients depend on chemical composition and temperature. The results are discussed in the light of previous results reported in the literature. Areas in need of further work are highlighted.

GRAPHICAL ABSTRACT



Handling Editor: P. Nash.

Address correspondence to E-mail: oliver.horst@rub.de

Introduction

Ni-based single-crystal superalloys (SXs) are used to manufacture turbine blades, which operate at temperatures above 1000 °C. They have to withstand a load spectrum, which includes creep, thermal fatigue and hot corrosion. Creep strength, the resistance against a slow but continuous accumulation of strain, is of utmost importance. It is well known that SXs rely for their strength on a microstructure, which consists of sub-micrometer cuboidal γ^2 -particles (crystal structure: ordered L_{12} -phase; volume fraction: 70 vol.%) which are separated by thin γ -channels (crystal structure: fcc; volume fraction: close to 30 vol.%), e.g., [1–4]. The crystal structures of both phases are similar, thus that on cooling from high temperatures the ordered γ^2 -particles can coherently precipitate in the γ -matrix. The lattice constants d of the two phases differ. In Ni-base single-crystal superalloys, one often finds: $d_{\gamma^2} < d_{\gamma}$. The associated lattice misfit results in an increase in elastic strain energy, e.g., [5, 6]. This misfit and some of its consequences, e.g., its effect on the shape of γ^2 -particles, on Peach–Köhler forces acting on channel dislocations, on rafting and on the formation of interfacial dislocation networks, have been and are still being discussed in the literature, e.g., [7–15]. The ordered γ^2 -particles represent obstacles to dislocation motion. They are not completely impenetrable, but it is more difficult for dislocations to move through the ordered γ^2 -phase than through the fcc γ -channels. The art of SX design partly relies on making it as difficult as possible for dislocations to cut into the γ^2 -phase to optimize creep strength. Making cutting difficult is associated with increasing antiphase boundary energies (APBs), e.g., [16–20], which result from one of the most prominent elementary mechanisms in crystal plasticity: the pairwise cutting of the γ^2 -phase, e.g., [21–23]. While in the literature there are disagreements as far as specific aspects of this cutting process are concerned, SX researchers from academia and industry believe that it is desirable to design alloys with a high γ^2 -volume fraction, a high γ^2 -solvus temperature and a chemical composition, which gives rise to high planar fault energies which affect the physical nature of APBs and stacking faults. The γ^2 -solvus temperature has been considered as especially important and has been highlighted as a reference

temperature in many scientific and technological SX publications, e.g., [24–31].

The present work takes a closer look at the thermodynamic properties of four SXs, ERBO/1 (with Re, a CMSX-4 type alloy) and three ERBO/15 variants (Re-free, with higher levels of Mo, Ti and W). It uses resonant ultrasonic spectroscopy (RUS) and dilatometry to measure elastic stiffnesses and thermal expansion coefficients as a function of temperature. It has recently been shown how these four alloys differ in terms of creep properties [32, 33].

The present work investigates how much large (ERBO/1 vs. ERBO/15) and small (three ERBO/15 variants) variations in alloy composition affect their thermoelastic properties. First objective: The comparison of two different alloys (large variation in alloy compositions) helps in the overall effort to move toward a superalloy single-crystal technology, where expensive and strategic alloy elements like Re, which are known to provide a high creep strength, are replaced by other elements without jeopardizing mechanical strength. Elastic and creep properties are both important in this respect. It has been proposed that this can be achieved by increasing the levels of Mo, Ti and W [34]. Further, elastic coefficients are needed in high-temperature engineering to design components, which need to withstand thermal fatigue loading. Therefore, an effort is made in the present work to measure elastic coefficients. Second objective: A detailed understanding of the role of individual alloy elements can only be obtained, when the effect of one particular element is studied. The comparison of the three ERBO/15 variants helps in this respect. Third objective: In particular, the potential of high-resolution dilatometry as a method for determining high γ^2 -solvus temperatures is explored. For this purpose, we compare experimental results for γ^2 -solvus temperatures obtained by high-temperature dilatometry with theoretical ThermoCalc calculations [35]. The quality of the ThermoCalc predictions is assessed by comparing its predictions for the chemical compositions of the γ - and γ^2 -phases obtained using 3D atom probe tomography (3D-ATP) [36] and transmission electron microscopy (TEM) [32]. To establish high-resolution measurements of thermal expansion as a method for determining γ^2 -solvus represents a significant progress in superalloy technology.

Table 1 Chemical composition (average composition) of the four SXs investigated in the present work. Concentrations are given in at.-%. Data from: ERBO/1 [36] (experimental), ERBO/15 and its derivatives [32, 34] (nominal)

Alloy	Al	Ti	Cr	Co	Mo	Hf	Ta	W	Re	Ni
ERBO/1	13.1	1.3	7.3	9.6	0.4	0.03	2.3	2.1	1.0	Base
ERBO/15	11.3	4.0	7.6	3.1	2.6	0.0	0.0	2.5	0.0	Base
ERBO/15-Mo	11.3	4.0	7.6	3.1	1.3	0.0	0.0	2.5	0.0	Base
ERBO/15-W	11.3	4.0	7.6	3.1	2.6	0.0	0.0	1.3	0.0	Base

The results are discussed in light of previous work published in the literature. Areas, which require further research, are highlighted.

Materials, experiments and methods

Materials: In the present work, four materials are investigated. Their nominal chemical compositions are listed in Table 1. ERBO/1 is a CMSX-4 type of alloy, details on processing, multiple step heat treatment and microstructure have been published elsewhere [32, 33, 36, 37]. ERBO/15 is a low-density Re-free single-crystal Ni-base superalloy, which has been developed by Rettig et al. [34] using a numerical thermodynamic multi-criteria optimization method. In the present work, we compare ERBO/15 with two leaner ERBO/15 variants, which contain less W and less Mo (ERBO/15-W and ERBO/15-Mo).

The heat treatment details of the four investigated alloys are presented in Table 2. While ERBO/1 was heat-treated by Doncasters Precision Castings in Bochum, the heat treatments of the ERBO/15 variants were performed in a custom-built vacuum heat treatment furnace from Carbolite Gero of type LHTM

100–200/16 1G. Detailed information about the heat treatment procedure is documented in [32] and [36].

Electron probe microanalysis (EPMA) was performed using an electron probe microanalyzer SX 50 for ERBO/1 and a field emission electron microprobe of type SXFiveFE for ERBO/15 and its two derivatives, both from Cameca. It is well known that during solidification, alloy elements of SXs can vary in their tendencies to partition to dendritic and interdendritic regions. Figure 1 presents the distributions of the elements Al, Ti, Mo and W in the microstructure of ERBO/15 in the as-cast condition (upper row, Fig. 1a–d) and after the homogenization heat treatment (lower row, Fig. 1e–h). The lower row of Fig. 1 shows that the large-scale chemical heterogeneity, associated with the partitioning tendencies of the alloy elements during solidification, can be lowered during the homogenization step (Table 2); however, it does not completely vanish as can be seen for W in Fig. 1h.

Scanning electron microscopy (SEM) investigations were performed using a Leo Gemini 1530 SEM from Carl Zeiss AG equipped with a field emission gun (FEG) operating at 12 kV and an inlens detector (working distance: 4.5mm, aperture: 30 mm).

Table 2 Heat treatment details of ERBO/1 [36] and ERBO/15 variants [32]

ERBO/1		
Homogenization	(B)	1563 K for 1 h $\xrightarrow{1\text{Kmin}^{-1}}$ 1573 K for 6 h $\xrightarrow{-150\text{Kmin}^{-1}}$ 1073 K $\xrightarrow{\text{air}}$ RT
Primary Age	(C1)	1413 K for 2 h $\xrightarrow{-150\text{Kmin}^{-1}}$ 1073 K $\xrightarrow{\text{air}}$ RT
Secondary Age	(C2)	1143 K for 16 h $\xrightarrow{-150\text{Kmin}^{-1}}$ 1073 K $\xrightarrow{\text{air}}$ RT
ERBO/15, ERBO/15-Mo, ERBO/15-W		
Homogenization	(B)	1573 K for 2 h $\xrightarrow{1\text{Kmin}^{-1}}$ 1583 K for 6 h $\xrightarrow{-700\text{Kmin}^{-1}}$ 873 K $\xrightarrow{\text{vacuum}}$ RT
Primary Age	(C1)	1313 K for 2 h $\xrightarrow{-700\text{Kmin}^{-1}}$ 873 K $\xrightarrow{\text{vacuum}}$ RT
Secondary Age	(C2)	1143 K for 16 h $\xrightarrow{-700\text{Kmin}^{-1}}$ 873 K $\xrightarrow{\text{vacuum}}$ RT

Figure 2 presents SEM micrographs of the eight material states, which were considered in the present work. The four as-cast materials states are presented in the upper row of Fig. 2. The fully heat-treated material states after the secondary aging treatment (Table 2) are shown in the lower row of Fig. 2.

Transmission electron microscopy (TEM) was used to analyze the local alloy chemistry of the two phases in the γ/γ^2 -microstructure. TEM was performed using a JEOL JSM-6490 (for ERBO/1) and a Tecnai G² F20 from FEI (for ERBO/15 and its derivatives), both equipped with a FEG operating at 200 kV and an EDAX analysis system. The procedure, which was used to measure phase compositions in the three ERBO/15 variants, is illustrated in Fig. 3. The picture in the middle of Fig. 3 shows a STEM micrograph taken in a $\langle 100 \rangle$ direction (multiple beam contrast). EDX spectra were taken at five γ -channel positions (1–5, as indicated) and in the centers of the four adjacent γ^2 -particles (positions 6–9). Each EDX spectrum was recorded with an electron beam diameter < 10 nm over a time period of 60 s. Compositions were calculated using the EDAX algorithm. The values for the two phases were obtained as the averages of the five channel measurements (analysis points 1 to 5) and the four particle measurements (analysis points 6 to 9). Examples of EDX spectra for the cross γ -channel (in orange, position 1) and for the

upper right γ^2 -particle (in green, position 7) are shown in the left and right diagrams as indicated.

For comparison, we use some of the local composition results reported by Parsa et al. [36], which were obtained by a local electrode atom probe (LEAPTM 3000X HR, Cameca Instruments) in voltage mode at a specimen base temperature of ~ 65 K.

Resonant ultrasound spectroscopy (RUS): In the present work, elastic stiffness coefficients as a function of temperature were determined with the aid of resonant ultrasound spectroscopy (RUS), e.g. [38, 39]. Precisely $\langle 100 \rangle$ oriented cuboidal specimens of target dimensions of about $8 \times 7 \times 6$ mm³ = 336 mm³ were obtained by combining Laue orientation with spark erosion machining as described in [40]. In the present work, RUS measurements were taken for ERBO/15 and its variants. For comparison, the data for ERBO/1 were taken from the work of Demtröder et al. [41]. All specimen dimensions are given in Table 3. For all specimens tested in the present work, there was good agreement between geometric densities ρ_G (calculated from sample weights and volumes) and the densities determined by the buoyancy method ρ_B (Table 3). Good surface qualities were established by grinding and diamond plate polishing.

In Fig. 4a, a typical RUS specimen is shown clamped in between two ceramic rods and the

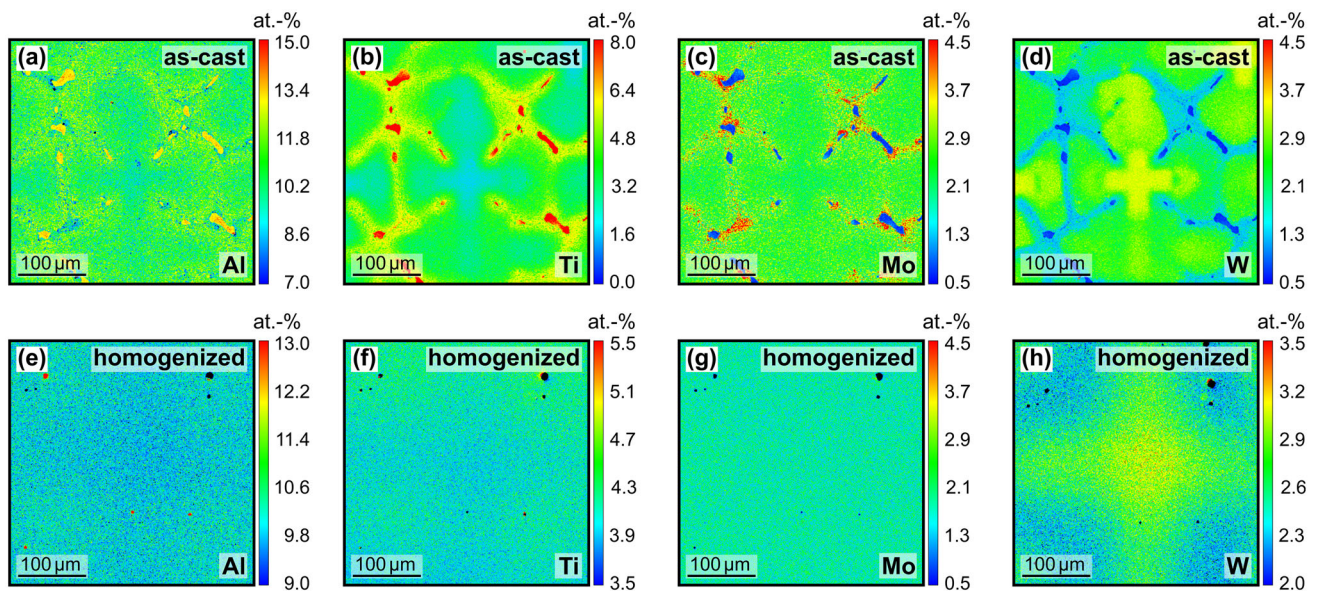


Figure 1 Electron probe microanalysis (EPMA) maps showing distribution of Al, Ti, Mo and W in the microstructures of ERBO/15. **a** Al—*as-cast*. **b** Ti—*as-cast*. **c** Mo—*as-cast*. **d** W—*as-cast*.

e Al—*homogenized*. **f** Ti—*homogenized*. **g** Mo—*homogenized*. **h** W—*homogenized*.

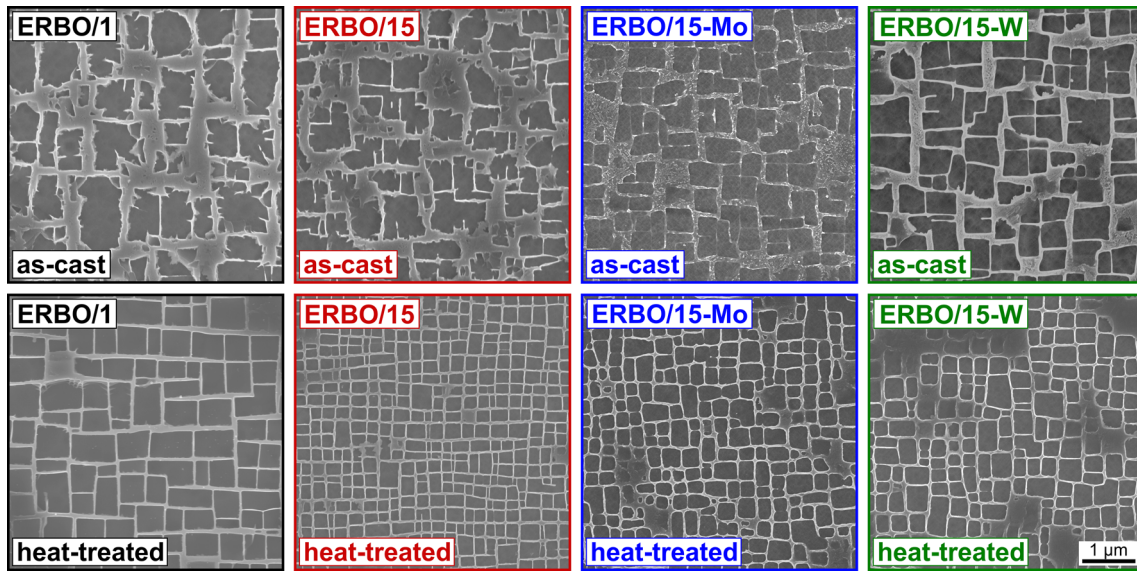


Figure 2 Secondary electron micrographs (dendritic region) of as-cast (A, first line) and heat-treated (C, second line) material states of ERBO/1, ERBO/15, ERBO/15-Mo and ERBO/15-W.

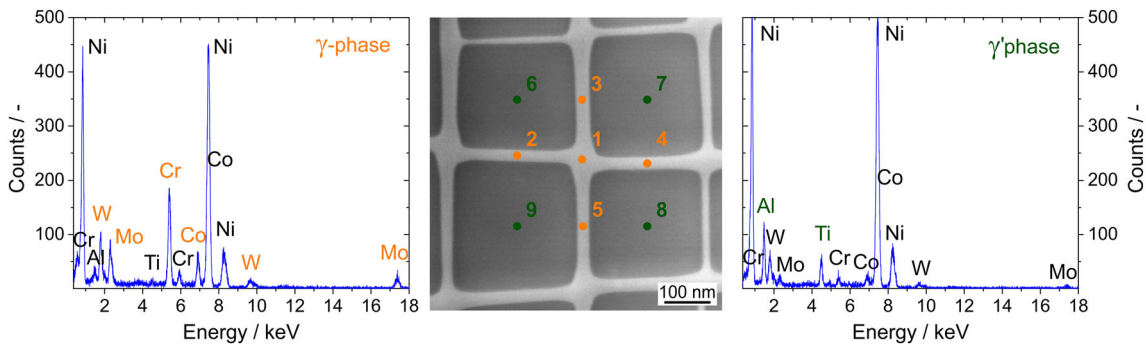


Figure 3 Examples for TEM EDX spectra from γ -channels and γ' -particles in ERBO/15. Center: STEM micrograph indicating nine locations where EDX measurements were taken. Left: EDX spectrum from γ -channel crossing (position 1 in central image).

Right: EDX spectrum from γ' -phase (position 7 in central image). Elements partitioning to the γ -matrix and γ' -cubes are highlighted in orange and green.

measurement thermocouple nearby. During the experiments, the thermocouple was not attached to the specimen but very close. Specimen and the relevant part of the thermocouple were in the temperature constant zone of the furnace.

For the experimental determination of resonance frequencies, freely vibrating samples are employed. The experimentally obtained resonance frequencies are related to the three independent elastic stiffness coefficients c_{11} , c_{12} and c_{44} of the pseudo-cubic crystal [38, 39, 41]. For data collection, a RUS apparatus built in-house was used. The system consisted of a frequency response analyzer (type FRA5087 from NF Corporation) in combination with a high-speed

amplifier (type BA4825 from NF Corporation) for signal generation and detection. The experiments were performed in the temperature range from 100 to 673 K using a Netzsch low-temperature furnace and a cascading temperature controller (type 2704 from Eurotherm). Resonance spectra of the samples were recorded in the range from 150 to 1000 kHz. In the case of ERBO/1, Demtröder et al. [41] studied the elastic properties in 50 K steps between room temperature and 1273 K. The ERBO/15 variants of the present work were investigated in 10 K steps between 100 and 673 K.

According to Demtröder et al. [41], the large-scale heterogeneities associated with the cast

Table 3 Dimensions l_i of cuboidal specimens used for resonant ultrasound spectroscopy investigations (RUS) and for dilatometry (DIL)

Alloy	ERBO/1 [41]		ERBO/15		ERBO/15-Mo		ERBO/15-W	
Sample code	KD010	KD011	JS207	JS208	JS211	JS212	JS209	JS210
l_1 / mm	5.464	5.480	5.868	5.900	5.858	5.884	5.802	5.836
l_2 / mm	6.479	6.476	6.962	6.987	6.798	6.882	6.915	6.837
l_3 / mm	7.501	7.505	8.120	7.972	8.110	7.976	8.051	7.978
V / mm ³	266	266	332	329	323	323	323	318
ρ_G / (g cm ⁻³)	8.70	8.69	8.29	8.34	8.18	8.25	8.13	8.13
ρ_B / (g cm ⁻³)	8.67	8.67	8.33	8.31	8.28	8.28	8.15	8.13
Method	RUS	DIL	RUS	DIL	DIL	RUS	DIL	RUS

The ERBO/1 specimen (from [41]) was fully heat-treated; the ERBO/15-type specimens (present work) were machined from the as-cast material states. Errors of sample dimensions are $\pm 2 \mu\text{m}$ and of densities are $\pm 0.03 \text{ g cm}^{-3}$

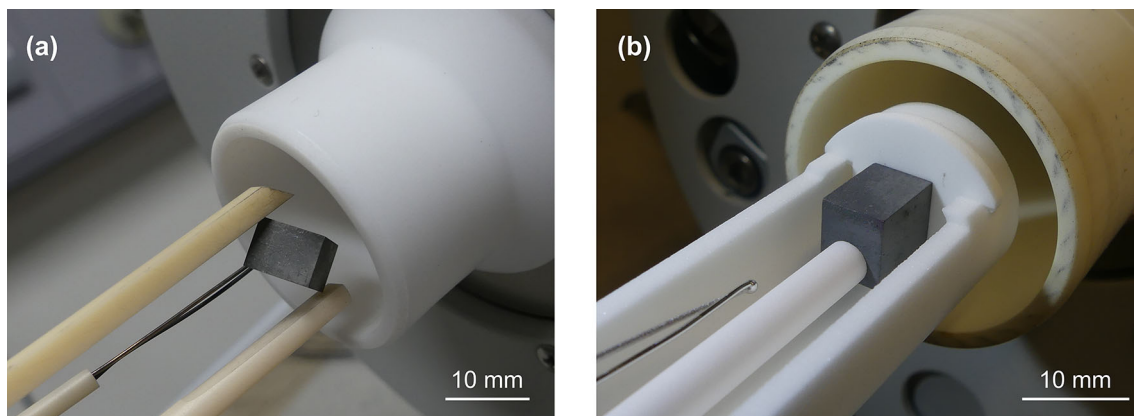


Figure 4 SX samples mounted prior to testing. **a** Arrangement corresponding to the high-temperature test condition of the RUS measurements. **b** Dilatometric measurement of thermal expansion

(DIL), thermocouple is positioned closer to the specimen during the experiment. For details, see text.

microstructure (dendrites and interdendritic regions) can influence the resonances with wave lengths of the order of the dendrite spacing. Following the procedure described by Demtröder et al. [41], elastic coefficients of all samples were refined on the basis of the 50 eigenmodes with the lowest frequencies (highlighted in gray in Fig. 5a–d) by a nonlinear least-squares fit procedure. Taking a closer look at the differences between the experimentally observed resonance frequencies f_{obs} and those calculated from the refined sample parameters f_{calc} at room temperature yields deviations between 0.33 and 0.6 kHz on average, which documents the good quality of the refinements. In Fig. 5, these differences are plotted as a function of the eigenmodes from the lowest to the highest resonance frequency. Demtröder et al. [41] have shown that this difference increases with decreasing sample size. Most importantly, good

results are obtained when the specimen dimensions exceed the mean spacing between dendrites by at least a factor of 10. The authors also concluded that average deviations of less than 2 kHz are acceptable. As can be seen in Fig. 5, the average scatter observed in the present work does not exceed this value.

Dilatometry (DIL): High-precision dilatometry was used to monitor the temperature dependence of the coefficient of thermal expansion α_{th} . The thermally induced strain ε_{th} , i.e. the relative change of sample length $\Delta L / L_0$ (L_0 : sample length at 293 K) with temperature, was measured between 100 and 1573 K using an inductive gauge dilatometer of type DIL402c from Netzsch as described in [41]. As can be seen in Fig. 4b (specimen clamped in between two ceramic rods, thermocouple close but not yet attached), the specimens used for the measurement of thermal expansion had the same geometry and

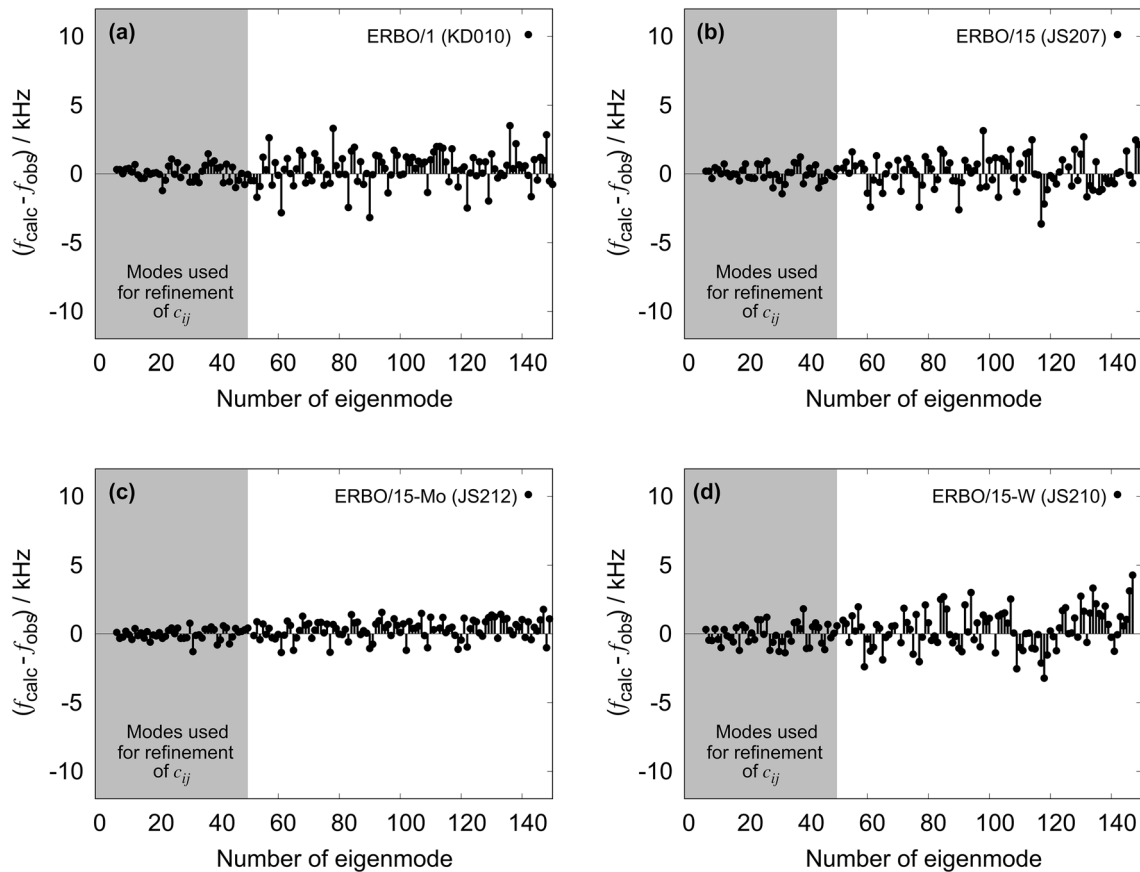


Figure 5 Scatter of $f_{calc} - f_{obs}$ between calculated and observed resonance frequencies of the first 140 eigenmodes of freely vibrating samples: **a** ERBO/1. **b** ERBO/15. **c** ERBO/15-Mo. **d** ERBO/15-W. For details regarding sample parameters, see Table 3.

crystallographic orientation as those taken for the assessment of the elastic stiffnesses, see Table 3. The dilatometer was calibrated with standard samples of the same lengths made of corundum. All experiments were performed in He-atmosphere at heating rates of 2 K/min. The coefficients of linear thermal expansion $\alpha_{th} = \partial \varepsilon_{th} / \partial T$ were determined as the first derivatives of the corresponding strain temperature curves. To this end, 40 (strain, temperature) data pairs within an interval of ± 1.5 K around each temperature T_i were approximated by a second-order polynomial from which $\alpha_{th}(T_i)$ was calculated.

Thermodynamic calculations: In a multicomponent alloy, phase stabilities depend on alloy chemistry, temperature and pressure [43–45]. Today, the CALPHAD method (CALPHAD—short for: CALculation of PHase Diagrams) originally developed by Kaufmann and Bernstein [45] can be used to calculate phase equilibria in multicomponent alloys [46, 47]. In the present work, ThermoCalc (a state-of-the-art

CALPHAD implementation) in combination with database TCNi8, version 2019b [35]) was used to calculate thermodynamic equilibria with a focus on γ^2 solvus temperatures and the chemical compositions of the γ - and the γ^2 phases. Additionally, liquidus and solidus temperatures as well as the γ^2 -volume fractions were calculated as a function of the temperature for all four alloys. These calculations are based on a homogeneous chemical distribution of alloy elements in our SX. In reality, there is a dendritic solidification with dendritic (D) and interdendritic (ID) regions containing different chemical compositions. However, as has been shown in [36], the differences in average chemical compositions between D and ID regions are accounted for by an adjustment of volume fractions, the γ -channels and the γ^2 -cuboids in both regions had the same composition. Therefore, no effort was made to differentiate between D and ID regions, as far as the chemical compositions of the two phases are concerned.

Results

Elastic properties: The elastic stiffnesses of pseudo-single-crystal ERBO/15 and its variants as obtained by the RUS method at room temperature are presented in Table 4. For comparison, data for ERBO/1 from the literature [41] have been added. Additionally, the elastic compliances s_{ij} have been calculated using the relations, which hold for materials with cubic symmetry.

$$\begin{aligned} s_{11} &= \frac{c_{11} + c_{12}}{(c_{11} - c_{12})(c_{11} + 2c_{12})}; \\ s_{12} &= \frac{-c_{12}}{(c_{11} - c_{12})(c_{11} + 2c_{12})}; \quad s_{66} = \frac{1}{c_{44}} \end{aligned} \quad (1)$$

The directional Young's or elastic modulus E equals the inverse of the longitudinal effect of the elastic compliances. With the direction of interest $\mathbf{u} = u_1\mathbf{e}_1 + u_2\mathbf{e}_2 + u_3\mathbf{e}_3$, where \mathbf{e}_i describes the basis vectors of a Cartesian reference system and the u_i are direction cosine, the E moduli for selected cubic directions are obtained by:

$$E^{-1}(\mathbf{u}) = s_{11}(u_1^4 + u_2^4 + u_3^4) + (2s_{12} + s_{66})(u_1^2u_2^2 + u_1^2u_3^2 + u_2^2u_3^2) \quad (2)$$

Selected values are presented in Table 4.

The temperature dependence of the elastic stiffnesses is shown in Fig. 6. Between 100 and 673 K, c_{11} , c_{12} and c_{44} decrease continuously with increasing temperature by about 8.5%, 6% and 13%, respectively. Temperature coefficients of the c_{ij} as determined by linear approximations to experimental data in the temperature range 273–673 K are given in Table 4. In order to describe the temperature dependence of the E moduli in the crystallographic directions $\langle 100 \rangle$, $\langle 110 \rangle$ and $\langle 111 \rangle$, the corresponding $E_{\langle uvw \rangle}$ data were approximated over the entire investigated temperature range by second-order polynomials of the type:

$$E_{\langle uvw \rangle}(T) = a_0 + a_1(T - T_0) + a_2(T - T_0)^2 \quad (3)$$

The corresponding parameters and their standard deviations as derived from the covariance matrix of the fully converged fit are given in Table 5. As an example, values for $E_{\langle 100 \rangle}$ of ERBO/1 (data from [41]) and the ERBO/15 variants (this work) are shown in Fig. 6d.

Dilatometric results: Thermal expansion results for the four investigated superalloys are presented in Figs. 7 and 8. The experimental strain curves $\varepsilon_{\text{th}} = f(T)$ are all characterized by well reproducible changes in slope at high temperatures. This becomes particularly evident when the thermal expansion coefficients $\alpha_{\text{th}} = f(T)$ are plotted as a function of

Table 4 Elastic properties of ERBO/1 (published in [41]) and the ERBO/15 variants at room temperature as determined by resonant ultrasound spectroscopy in this work: c_{ij} elastic stiffness coefficients, s_{ij} elastic compliances [cf. Eq (1)], $E_{\langle uvw \rangle}$ elastic moduli [cf. Eq (2)]

Alloy	ERBO/1-C	ERBO/15-A	ERBO/15-Mo-A	ERBO/15-W-A
Sample code	KD010	JS207	JS212	JS210
$\rho_G / (\text{g cm}^{-3})$	8.70(2)	8.33	8.27	8.13
c_{11} / Pa	247.8(1)	249.2(1)	245.1(1)	243.7(1)
c_{12} / GPa	156.7(1)	157.4(1)	152.4(1)	151.5(1)
c_{44} / GPa	131.2(2)	129.7(2)	129.3(2)	129.6(2)
$\partial c_{11} / \partial T / \text{MPa K}^{-1}$	-36(2)	-40.6(3)	-41.8(3)	-39.2(3)
$\partial c_{12} / \partial T / \text{MPa K}^{-1}$	-13(2)	-19.0(2)	-19.7(3)	-16.8(3)
$\partial c_{44} / \partial T / \text{MPa K}^{-1}$	-32.6(5)	-31.9(1)	-32.2(2)	-32.4(1)
$\Delta f_{\text{av}} / \text{kHz}$	0.51	0.44	0.33	0.60
$\Delta f_{\text{max}} / \text{kHz}$	1.71	1.45	1.29	1.28
s_{11} / TPa^{-1}	7.911	7.857	7.796	7.846
s_{12} / TPa^{-1}	-3.064	-3.041	-2.989	-3.008
s_{44} / TPa^{-1}	7.621	7.712	7.735	7.716
$E_{\langle 100 \rangle} / \text{GPa}$	126.4	127.3	128.3	127.5
$E_{\langle 110 \rangle} / \text{GPa}$	231.0	230.7	230.6	230.0
$E_{\langle 111 \rangle} / \text{GPa}$	319.0	316.3	314.0	314.3

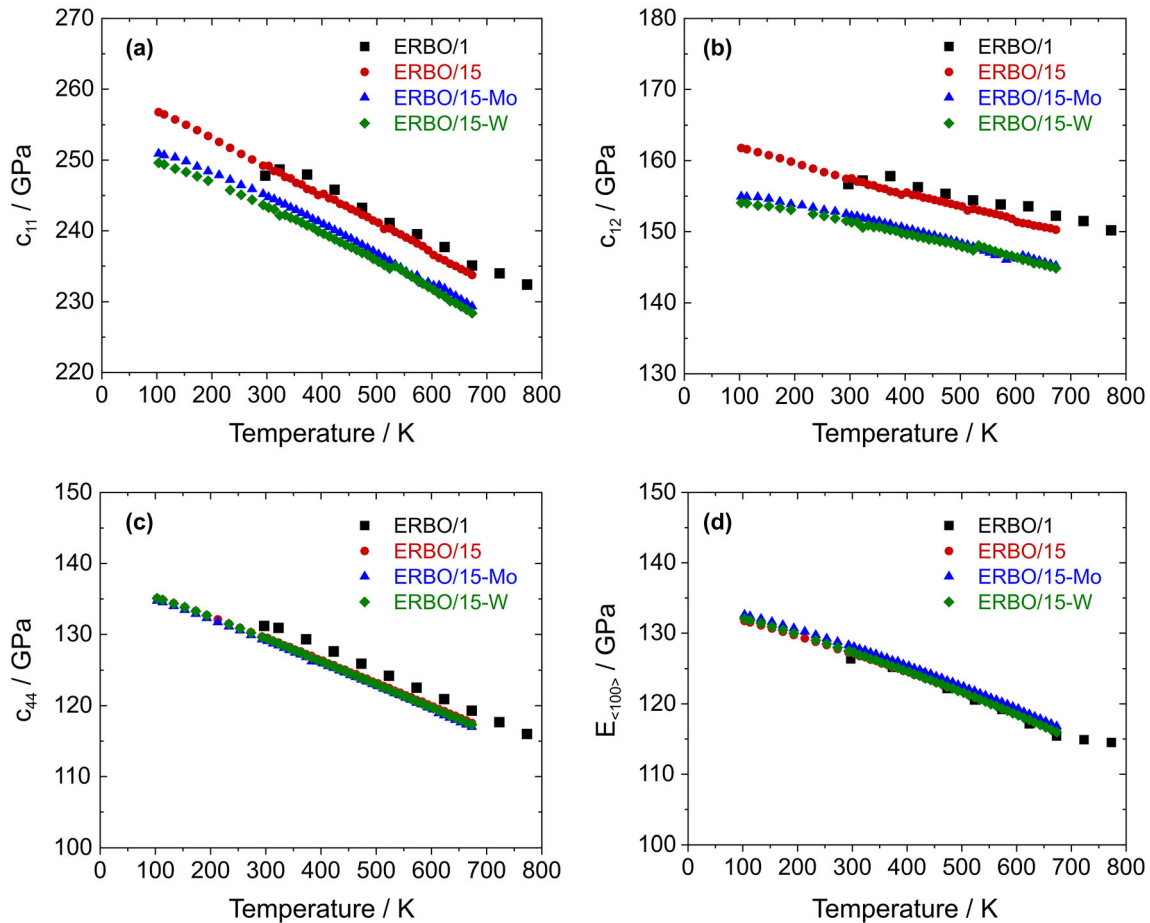


Figure 6 Elastic properties of the investigated alloys as a function the temperature. **a** Longitudinal elastic stiffness c_{11} . **b** Transverse interaction coefficients c_{12} . **c** Shear resistance c_{44} . **d** Elastic modulus $E_{\langle 100 \rangle}$ along $\langle 001 \rangle$.

temperature. These curves exhibit a sharp maximum of the thermal expansion coefficient at high temperatures. In Fig. 7, thermal strains and thermal expansion coefficients of the as-cast and fully heat-treated ERBO/15-W are shown.

It can be seen that the $\alpha_{th}(T)$ peak positions of the as-cast and heat-treated materials are close, the peak temperature of the heat-treated material is only 12 K higher than that of the as-cast material. ERBO/1 was investigated in the heat-treated material state. In the case of the ERBO/15 variants, the as-cast material state was analyzed.

ThermoCalc predictions and alloy compositions: ThermoCalc was used to calculate equilibrium phase fractions for all investigated alloys, based on the chemical alloy compositions given in Table 1. These are presented as a function of temperature in Fig. 9. While in ERBO/1 three thermodynamically stable TCP-phases (μ -, σ - and R-phase) are formed at equilibrium, only μ -phase is formed in ERBO15

and its derivatives. With increasing temperature, the TCP and γ^2 -phase fractions decrease, while the fraction of the γ -phase increases. In Table 6, the calculated solvus (T_{solvus}), solidus ($T_{solidus}$), liquidus ($T_{liquidus}$) temperatures together with the γ^2 -phase fractions at 873 K and 1323 K taken from the curves presented in Fig. 9 are listed. It becomes apparent that especially the calculated γ^2 -solvus temperature for ERBO/1 is about 50 K higher than the solvus temperatures of ERBO/15 and its derivatives. While the calculated solidus temperatures are quite similar, the liquidus temperature of ERBO/1 is the highest of all four alloys. Also, the calculated γ^2 -phase fraction $f_V^{\gamma^2}$ at 873 K (74 vol.%) and 1323 K (56 vol.%) is the highest in the case of ERBO/1. When the Mo or W content in ERBO/15 is reduced (balanced by an increase in Ni), the calculated solidus and liquidus temperatures decrease. The reductions result in higher γ^2 -phase fractions at 873 K (+ 1 vol.%) but lower γ^2 -phase fractions at 1323 K (−3 vol.%).

Table 5 Coefficients of second-order polynomials according to Eq. 3 describing the temperature dependence of selected elastic moduli in the investigated temperature range ΔT . Reference temperature $T_0 = 295$ K. ERBO/1 data were taken from [41]

Alloy	Direction	$\Delta T / \text{K}$	a_0 / GPa	$a_1 / \text{MPa K}^{-1}$	$a_2 / \text{kPa K}^{-2}$
ERBO/1	<100>	200–1400	127.2(2)	−22.9(9)	−19.0(8)
	<110>	200–1400	231.8(4)	−43(2)	−23(2)
	<111>	200–1400	319.5(7)	−62(3)	−15(3)
ERBO/15	<100>	100–673	127.3(1)	−25.1(1)	−11.6(3)
	<110>	100–673	230.7(1)	−47.9(1)	−13.4(4)
	<111>	100–673	316.2(2)	−68.4(2)	−9.5(6)
ERBO/15-Mo	<100>	100–673	128.2(1)	−25.4(1)	−12.9(2)
	<110>	100–673	230.5(1)	−47.5(1)	−16.8(3)
	<111>	100–673	313.9(4)	−66.8(2)	−15.9(7)
ERBO/15-W	<100>	100–673	127.5(1)	−26.0(1)	−11.4(2)
	<110>	100–673	229.9(1)	−48.2(1)	−14.2(3)
	<111>	100–673	314.1(2)	−67.4(2)	−12.3(6)

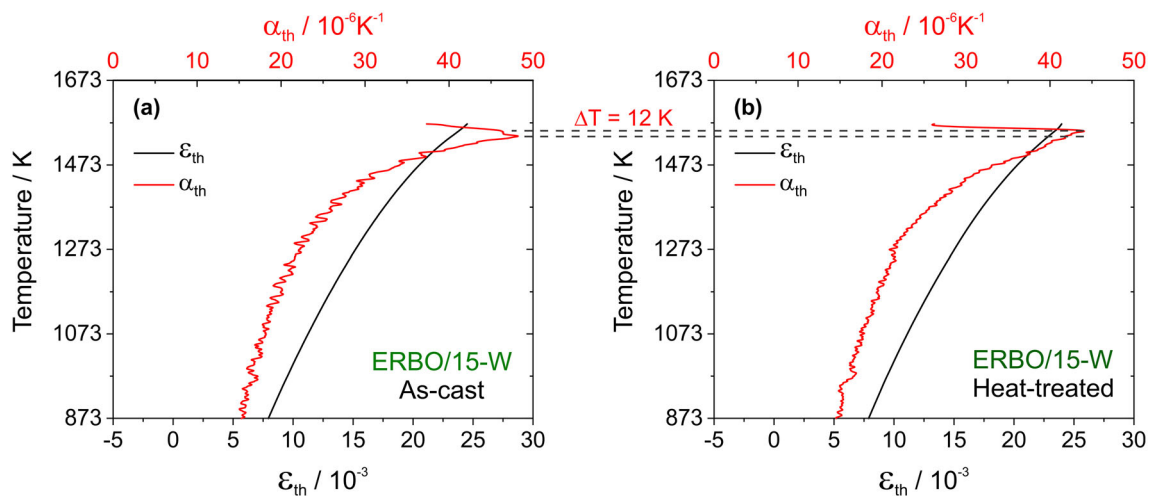


Figure 7 Thermal strain ε_{th} and thermal expansion coefficient α_{th} curves for as-cast and heat-treated ERBO/15-W.

Calculated and measured phase compositions: The compositions of the γ - and γ^2 -phase (c_γ and c_{γ^2}) in the four investigated alloys were measured with 3D APT (ERBO 1) [36] and with TEM-EDX (ERBO 15 and derivatives) [32]. The experimental results for the two phases are presented in Tables 7 (γ -phase) and 8 (γ^2 -phase). Tables 7 and 8 also contain ThermoCalc predictions obtained for temperatures at 1143 K (temperature of second precipitation treatment step for all alloys), at 1413 K and 1583 K (ERBO/1; temperature of first precipitation treatment step and homogenization, respectively) and at 1313 K and 1583 K (ERBO/15 variants; temperature of first precipitation treatment step and homogenization, respectively). Since the γ -phase exhibits a smaller volume fraction than the γ^2 -phase, changes in its chemical composition are more pronounced. In Figs. 10 and 11, we present

chemical compositions for the γ -phase from Table 7 as pie charts. Figure 10 shows experimental data, which were measured in all four heat-treated alloys prior to creep. ThermoCalc predictions obtained for the γ -phases of ERBO/1 (1143, 1413 and 1583 K) and for ERBO/15 (1143, 1313 and 1583 K) are presented in Fig. 11.

The data presented in Table 7 and Figs. 10 and 11 (γ -phase) and in Table 8 (γ^2 -phase, data presented without graphics) show that increasing temperatures result in increasing amounts of Ti, Al and Ta and simultaneously decreasing amounts of Cr, Co, W and Re for ERBO/1 in the γ -phase. As can be seen in the ThermoCalc results presented in Fig. 11, the amount of the base element Ni is increasing with increasing temperature in ERBO/1. In contrast, it decreases with increasing temperature in ERBO/15. The

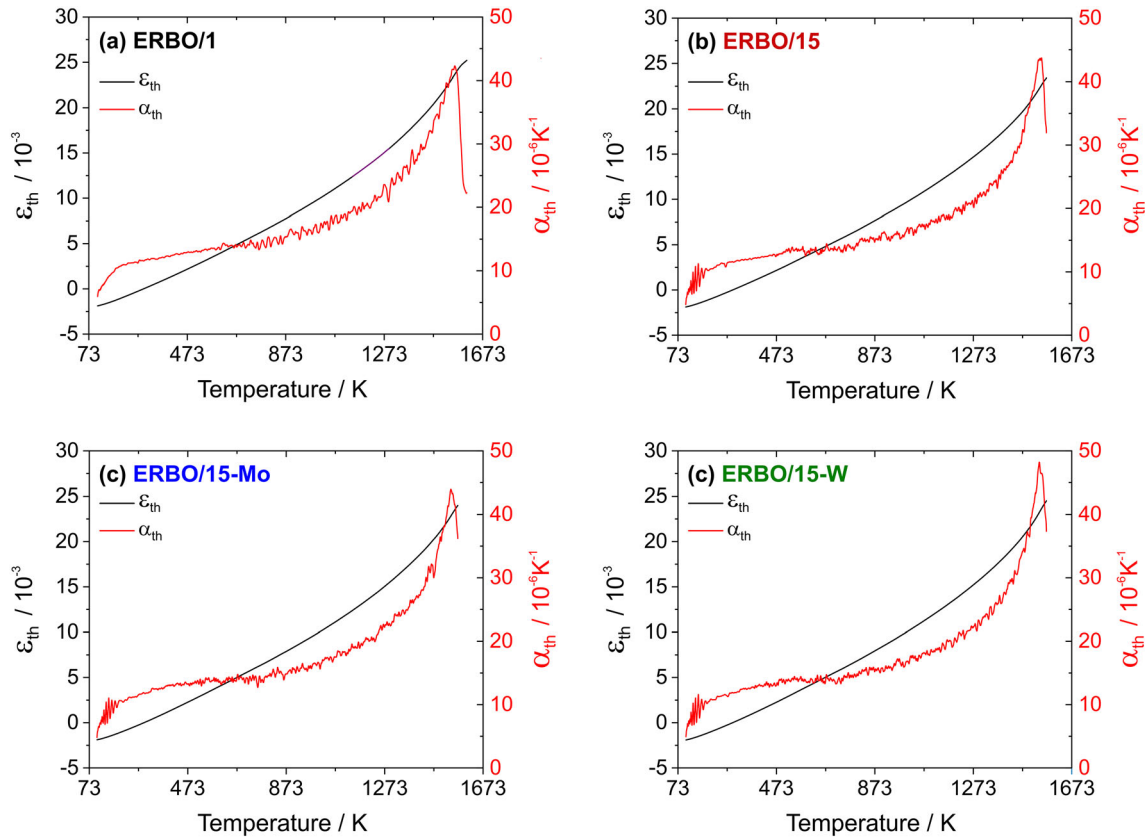


Figure 8 Thermal strain and thermal expansion as a function of temperature for the four alloys investigated in the present work. **a** ERBO/1. **b** ERBO/15. **c** ERBO/15-Mo. **d** ERBO/15-W. For details, see text.

thermodynamic data for the γ - and the γ' -phases in Table 7 (and Figs. 10 and 11) and Table 8, respectively, further show that the ThermoCalc data for 1143 K (temperature of last precipitation treatment of experimental alloys) and experimentally determined data are not in full agreement but reasonably close to each other for both alloy systems. Only in the case of ERBO/15, the element Mo shows a significantly lower value in the calculation at 1143 K (1.0 at.%) than in the experiment (4.4 at.%).

Discussion

Elastic stiffnesses: As can be seen in Fig. 6a–c, all elastic stiffnesses decrease with increasing temperature. This is mainly a consequence of the anharmonicity of the lattice potential. With increasing temperature, the increasing thermal vibrations lead to larger bond distances, which result in a decrease in bonding interaction and thus in a decrease in elastic stiffnesses. The elastic behavior of ERBO/1 and

ERBO/15 is almost identical, whereas the results for the leaner ERBO/15 variants for c_{11} and c_{12} fall slightly short. This does not significantly affect the elastic moduli $E_{\langle 100 \rangle}$, which all are very close (Fig. 6d). As can be seen in Table 9, individual alloy elements of SX differ in size, crystal structure, Young's modulus, electronegativity and melting point [48–51]. Figure 6d shows that the changes in alloy chemistry considered in the present work do not strongly affect elastic properties. This is in line with the conclusions drawn by Demtröder et al. [41], who showed that even larger variations of alloy compositions than considered in the present work do not strongly affect the elastic properties of SX. The elastic behavior of a single crystal directly reflects the anisotropy of its bonding system. The latter is mainly controlled by type, number and spatial arrangement of nearest-neighbor contacts in the crystal structure. Since the structures of Ni-base SX (including γ/γ' -microstructures) as well as their main chemical compositions (> 62 at.-% Ni, > 11 at.-% Al) differ only slightly, the interactions are dominated by Ni–

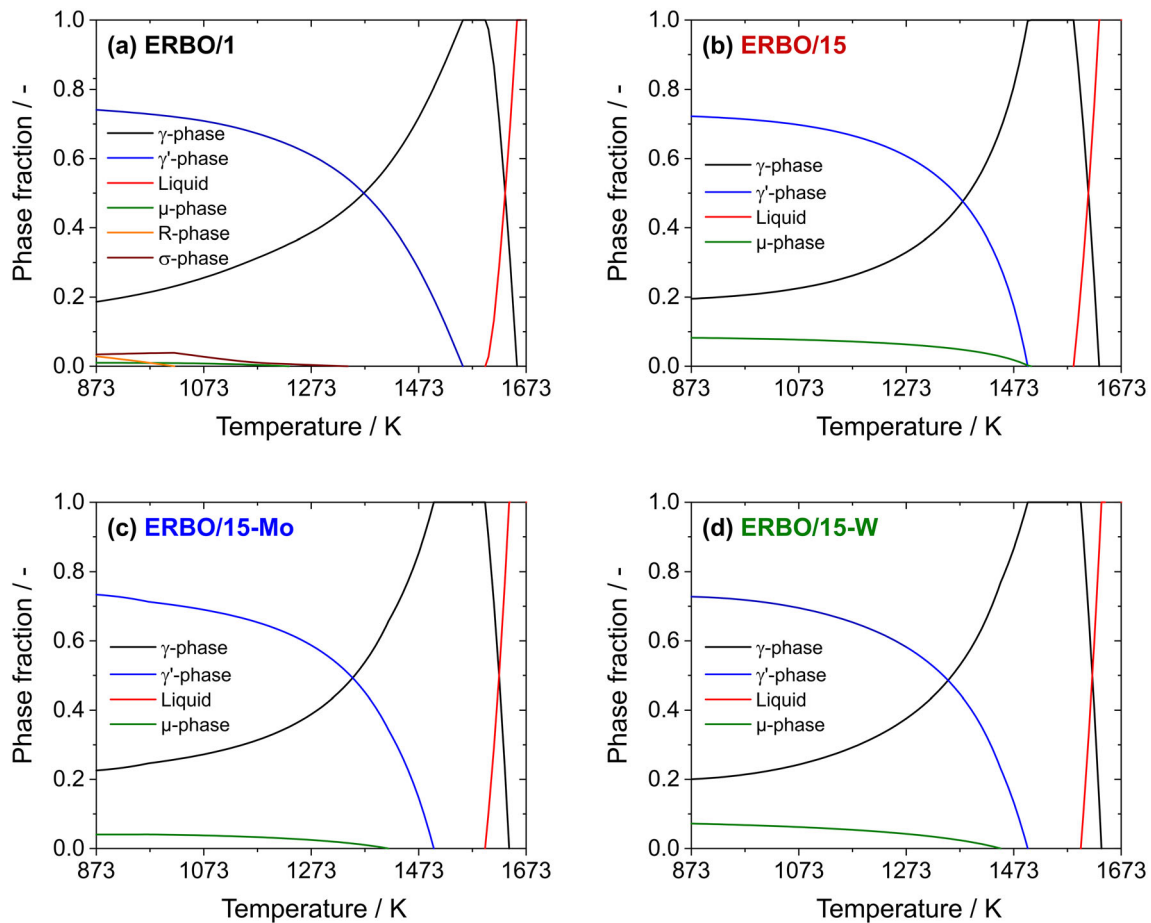


Figure 9 Equilibrium diagrams of the four investigated alloys showing the phase fraction of γ , γ' , liquid, μ , R and σ as a function of temperature. **a** ERBO/1. **b** ERBO/15. **c** ERBO/15-Mo. **d** ERBO/15-W. For details, see text.

Table 6 Characteristic temperatures calculated for the average chemical composition of the four alloys investigated in the present work

Alloy	T_{solvus} / K	T_{solidus} / K	T_{liquidus} / K	$\gamma'_{873K} / \text{vol.}\%$	$\gamma'_{1323K} / \text{vol.}\%$
ERBO/1	1555	1597	1656	74.10	56.28
ERBO/15	1506	1584	1632	72.25	55.82
ERBO/15-Mo	1501	1597	1641	73.36	53.25
ERBO/15-W	1499	1598	1636	72.77	52.63

T_{solvus} , T_{solidus} and T_{liquidus} : γ' -solvus, solidus and liquidus temperatures as predicted by ThermoCalc. γ'_{873K} and γ'_{1323K} : volume fraction of γ' -phase at 873 K and 1323 K by ThermoCalc

Ni and Ni–Al contacts, leading to only small variations of the macroscopic elastic stiffnesses [42].

Thermal expansion and γ' -solvus temperatures: Thermal expansion is associated with a material's tendency to change its volume with increasing temperature. In a crystal, this is associated with an increasing vibrational energy of the atoms and the non-harmonic shape of the lattice potential. According to the Grüneisen relation, $\alpha(T)$ is proportional to the heat capacity; thus, the thermal strain $\varepsilon(T)$ can be

described by an integrated form of the Einstein model [52, 53]:

$$\varepsilon(T) = \varepsilon_0 + \alpha_h \cdot \frac{\theta_E}{-1 + e^{\theta/T}} \quad (4)$$

ε_0 represents the initial strain at 0 K, α_h denotes the high-temperature limit of the thermal expansion coefficient, and θ_E is the equivalent of the Einstein temperature. The first derivative with respect to temperature yields the thermal expansion coefficient:

Table 7 Experimental (EDX STEM) and calculated (ThermoCalc [35]) chemical compositions obtained for the γ -phase of ERBO/1 and of ERBO/15 and its derivatives in at.-%

	Al	Ti	Cr	Co	Mo	Hf	Ta	W	Re	Ni
ERBO/1										
APT [36]	2.5	0.1	22.2	20.4	0.8	0.00	0.1	3.7	4.6	Base
ThermoCalc (1143 K)	4.2	0.1	17.2	20.9	0.5	0.00	0.2	4.0	2.1	Base
ThermoCalc (1413 K)	9.9	0.9	10.7	13.3	0.5	0.01	1.3	2.8	1.4	Base
ThermoCalc (1583 K)	12.6	1.3	7.7	9.9	0.4	0.03	2.2	2.1	1.0	Base
ERBO/15										
TEM [32]	1.8	0.5	19.8	6.0	4.4	–	–	3.0	–	Base
ThermoCalc (1143 K)	4.5	0.8	13.3	4.7	1.0	–	–	3.5	–	Base
ThermoCalc (1313 K)	7.0	1.8	11.7	4.1	1.8	–	–	3.0	–	Base
ThermoCalc (1583 K)	11.3	4.0	7.6	3.1	2.6	–	–	2.5	–	Base
ERBO/15-Mo										
TEM [32]	1.9	0.6	19.8	5.9	2.6	–	–	3.1	–	Base
ThermoCalc (1143 K)	4.2	0.7	14.7	4.9	0.7	–	–	4.5	–	Base
ThermoCalc (1313 K)	6.9	1.8	12.5	4.2	1.4	–	–	3.7	–	Base
ThermoCalc (1583 K)	11.3	4.0	7.6	3.1	1.3	–	–	2.5	–	Base
ERBO/15-W										
TEM [32]	2.3	0.6	18.8	6.1	4.4	–	–	2.1	–	Base
ThermoCalc (1143 K)	5.0	0.8	13.7	4.7	2.0	–	–	1.1	–	Base
ThermoCalc (1313 K)	7.3	1.7	12.0	4.1	2.9	–	–	1.4	–	Base
ThermoCalc (1583 K)	11.3	4.0	7.6	3.1	2.6	–	–	1.3	–	Base

The calculations were performed for three temperatures as indicated.

Table 8 Experimental (EDX STEM) and calculated (ThermoCalc [35]) chemical compositions obtained for the γ' -phase of ERBO/1 and of ERBO/15 and its derivatives in at.-%

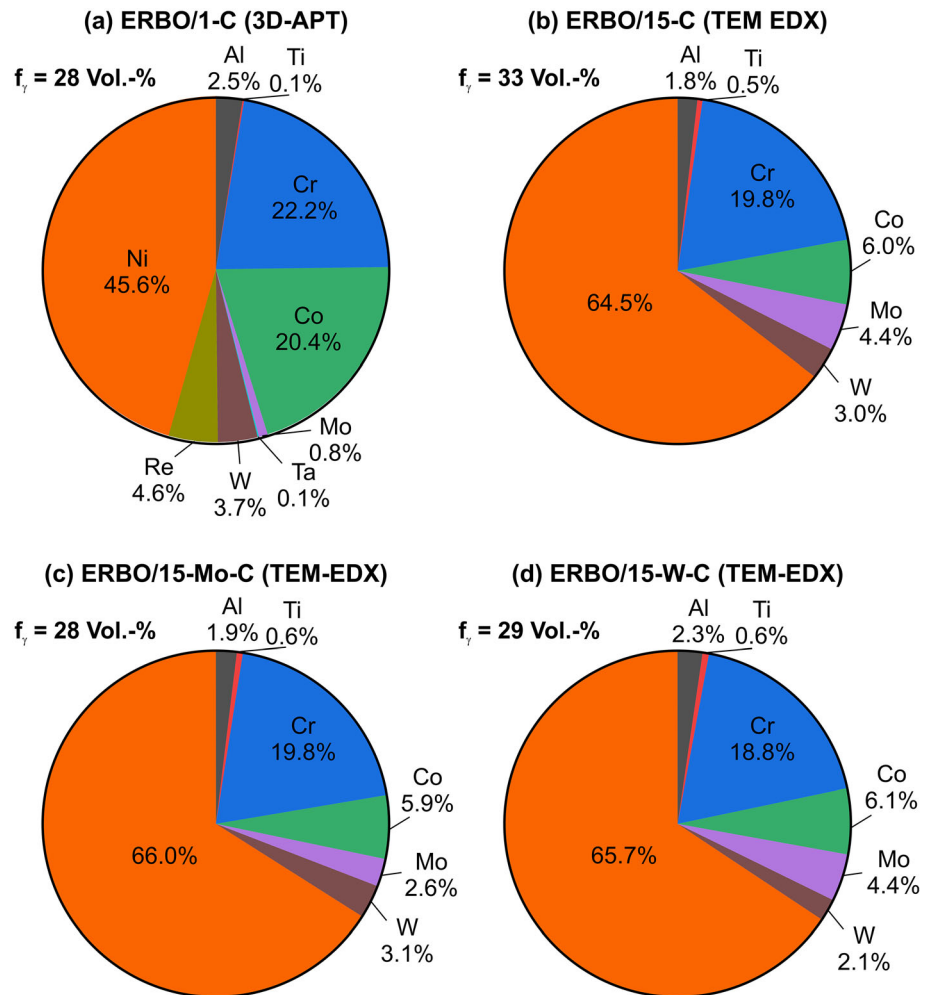
	Al	Ti	Cr	Co	Mo	Hf	Ta	W	Re	Ni
ERBO/1										
APT [36]	16.7	1.6	2.0	6.0	0.3	0.03	3.3	2.0	0.2	Base
ThermoCalc (1143 K)	17.2	1.9	2.5	4.2	0.1	0.05	3.2	0.8	0.1	Base
ThermoCalc (1413 K)	17.2	1.9	2.8	4.2	0.1	0.07	3.7	0.9	0.2	Base
ThermoCalc (1583 K)	–	–	–	–	–	–	–	–	–	–
ERBO/15										
TEM [32]	13.9	4.2	1.0	1.2	0.8	–	–	1.2	–	Base
ThermoCalc (1143 K)	15.0	5.6	3.1	2.0	0.2	–	–	0.7	–	Base
ThermoCalc (1313 K)	15.3	5.9	2.7	2.0	0.3	–	–	0.8	–	Base
ThermoCalc (1583 K)	–	–	–	–	–	–	–	–	–	–
ERBO/15-Mo										
TEM [32]	11.1	4.4	1.8	2.2	0.6	–	–	1.0	–	Base
ThermoCalc (1143 K)	15.1	5.7	3.2	2.1	0.1	–	–	0.9	–	Base
ThermoCalc (1313 K)	15.2	5.9	2.9	2.0	0.2	–	–	1.0	–	Base
ThermoCalc (1583 K)	–	–	–	–	–	–	–	–	–	–
ERBO/15-W										
TEM [32]	13.8	4.3	1.8	2.0	1.2	–	–	0.7	–	Base
ThermoCalc (1143 K)	14.9	5.7	3.2	2.0	0.5	–	–	0.2	–	Base
ThermoCalc (1313 K)	15.2	6.1	2.7	2.0	0.5	–	–	0.4	–	Base
ThermoCalc (1583 K)	–	–	–	–	–	–	–	–	–	–

The calculations were performed for three temperatures as indicated.

$$\alpha(T) = \frac{\partial \varepsilon}{\partial T} = \alpha_h \cdot \left(\frac{\theta_E}{T}\right)^2 \cdot \frac{e^{\theta/T}}{(-1 + e^{\theta/T})^2} \quad (5)$$

The Einstein model usually provides a good approximation of heat capacity and thermal expansion at temperatures above about $\theta_E/2$. In the case of the superalloys investigated in this work, the Einstein

Figure 10 Average chemical compositions of the γ -phase obtained by TEM [32] and APT [36] in the four alloys considered in the present work. **a** ERBO/1-C (3D-APT, [36]). **b** ERBO/15-C (TEM, [32]). **c** ERBO/15-Mo-C (TEM, [32]). **d** ERBO/15-W-C (TEM, [32]). Volume fractions are indicated.



approach describes well the observed thermal strains and thermal expansion coefficients up to about 800 K with θ_E varying between 396 and 412 K (Fig. 12a, c). However, at higher temperatures significant differences occur as expressed in Fig. 12a by the thermal excess strain, which represents the difference between the experimental thermal strain $\varepsilon_{\text{exp}}(T)$ (black curve) and the extrapolated strain $\varepsilon_{\text{fit}}(T)$ (red curve, Eq. 3) determined by fitting an Einstein model to $\varepsilon_{\text{exp}}(T)$ below 800 K. The experimental curve further undergoes a change of slope, which can be better appreciated considering its first derivative $\alpha_{\text{exp}}(T)$, black curve in Fig. 12c. In Fig. 12b, $\Delta\varepsilon^*(T)$ (black curve) is presented together with the evolution of the γ -volume fraction $f_\gamma(T)$ (red curve) as predicted by ThermoCalc. It can be clearly seen that both curves show similar trends, which is even more evident for their first derivatives (Fig. 12d). This strongly suggests that the

temperatures, where changes of slope of the ε_{th} -curves are detected, i.e., where the $\alpha_{\text{th}}(T)$ -curves show a sharp peak, represent γ^2 -solvus temperatures. Similar effects have been reported for ternary Ni–Fe–Al alloys [54], CMSX-2 [55] and Co-based alloys [56, 57].

Figure 13 schematically illustrates how the experimentally observed thermal expansions can be rationalized. In a first-order approximation, one can assume that the thermal expansions of the two isolated phases each follow an Einstein model (Eq. 5). Different model parameters result in the fact that at high temperatures, the γ -phase (green curve) reaches significantly higher values than the γ^2 -phase (blue curve). The red line schematically illustrates the experimental data for a superalloy, which contains both phases (Fig. 3). The thermal expansion of the γ^2 phase (high initial γ^2 volume fractions close to 70%) dominates for $T < 800$ K. Starting at about 800 K, the gradual dissolution of the γ^2 -precipitates and the

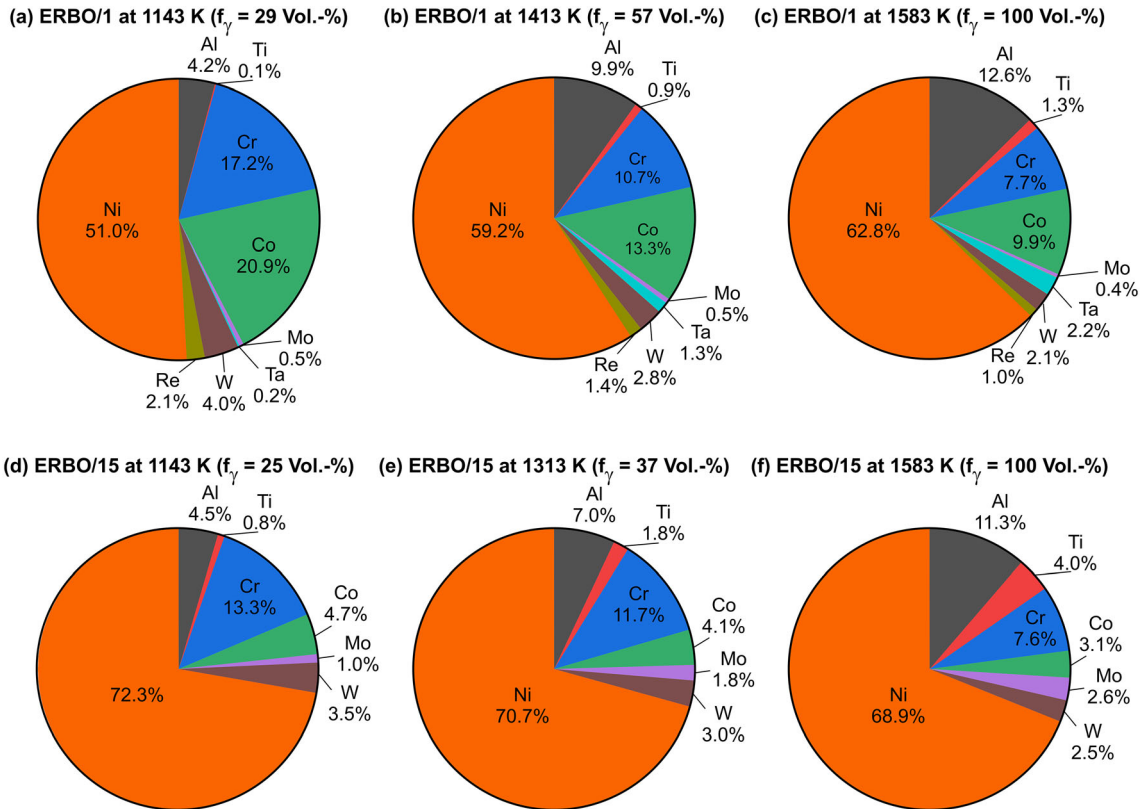


Figure 11 Average chemical compositions of the γ -phase calculated with ThermoCalc. **a, b and c:** ERBO/1. **d, e and f** ERBO/15-C. ERBO 1: **a** 1143 K. **b** 1413 K. **c** 1583 K. ERBO 15: **d** 1143 K. **e** 1313 K. **f** 1583 K. Volume fractions are indicated.

Table 9 Physical properties of the alloy elements of ERBO1 and ERBO15 and its derivatives [48–51]

	Al	Ti	Cr	Co	Mo	Hf	Ta	W	Re	Ni
Atomic radius / pm	125	140	140	135	145	155	145	135	135	135
Crystal structure	fcc	hcp	bcc	hcp	bcc	hcp	bcc	bcc	hcp	fcc
Young’s modulus / GPa	70	116	279	209	329	78	186	411	463	200
Electronegativity	1.61	1.54	1.66	1.88	2.16	1.30	1.50	2.36	1.9	1.91
Melting point / K	933	1941	2180	1768	2896	2506	3290	3695	3459	1728

corresponding increase in the volume fraction of the γ -phase (Fig. 12b) are associated with an adjustment of the chemical equilibrium compositions of the two phases. The resulting changes in unit cell dimensions and γ/γ^2 -volume fraction ratios cause the sharp peak in the experimentally measured thermal expansion close to T_{solvus} (Figs. 7, 8, 12c and d). About 50% of the excess strain $\Delta\varepsilon^*$ shown in Fig. 12a can be rationalized by the decreasing effect of the lattice misfit (estimate for ERBO15 and its variants: 5×10^{-3}), which provides additional contributions to the thermal strain. The remaining part of $\Delta\varepsilon^*$ is probably related to changes of the unit cell dimensions of both

phases related to an increase in configurational entropy. Additionally, the volume fraction of the γ -phase, which shows a higher coefficient of thermal expansion than the γ^2 -phase, increases with increasing temperature. This is in line with experimental data from the literature on the thermal expansion of isolated γ - and γ^2 -phases of CMSX-4 [58] and on a small step-like increase in heat capacity around about 870 K in CMSX-4 reported in [59].

With increasing temperature the vacancy density increases, as was reported for Al in the seminal work of Simmons and Balluffi [60]. However, this effect is usually very small and increases exponentially up to

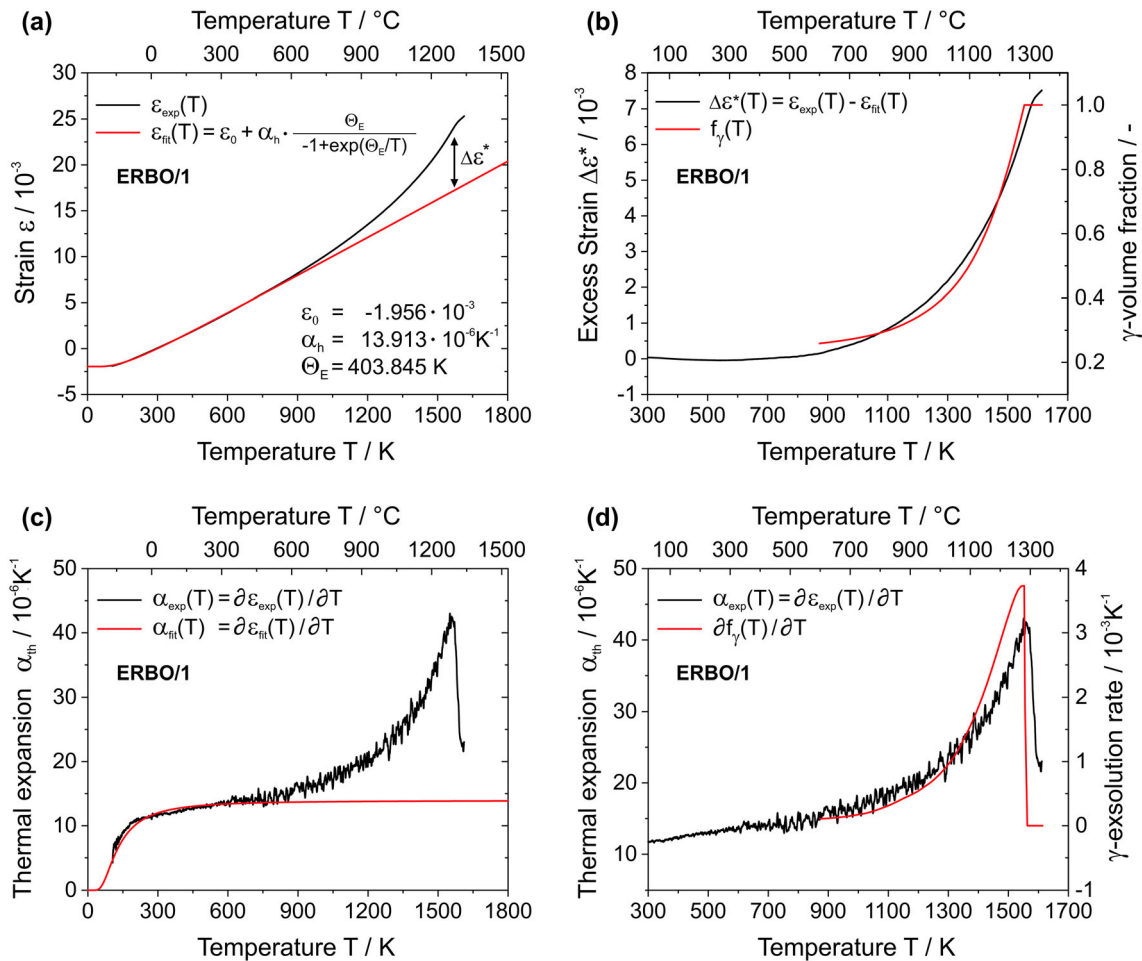


Figure 12 Rationalization of the correlation between thermal expansion and γ -volume fraction. **a** Experimental and fitted thermal strains, $\varepsilon_{\text{exp}}(T)$ and $\varepsilon_{\text{fit}}(T)$. **b** Evolution of the excess strain $\Delta\varepsilon^*(T)$ and γ -volume fraction $f_\gamma(T)$. **c** First derivatives of

experimental and fitted thermal strains (thermal expansion coefficients, $\alpha_{\text{exp}}(T)$ and $\alpha_{\text{fit}}(T)$). **d** First derivatives of $\varepsilon_{\text{exp}}(T)$ - (experimental data) and $f_\gamma(T)$ -curves. For details, see text.

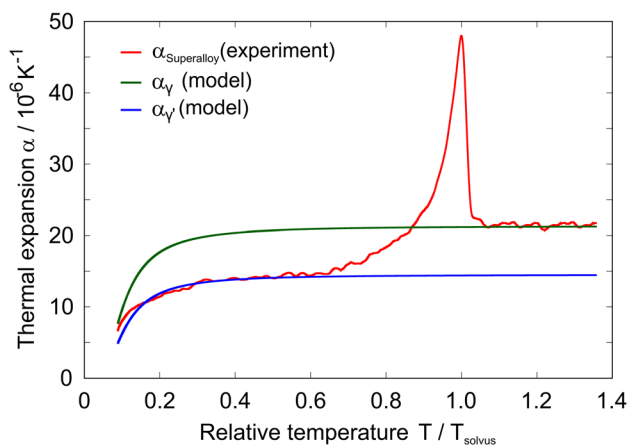


Figure 13 Schematic interpretation of thermal expansion results in terms of the Einstein model. For details, see text.

the melting temperature of the material. It is not related to the sharp peak observed in the experimental $\alpha_{\text{th}}(T)$ -curves. Similar effects have been reported for example for the order/disorder transformations in CuAu [61] and Ag₃Mg [62].

The dilatometric results of Fig. 8 and the CALPHAD predictions of Fig. 9 are combined in Fig. 14. The dilatometric curves exhibit a sharp maximum of thermal expansion at high temperatures, which for ERBO/1-C (1557 K) coincides with the γ^2 -solvus temperature (1555 K) predicted by ThermoCalc (Fig. 14a). However, for all three as-cast ERBO/15 variants, the $\alpha_{\text{th}}(T)$ -maxima are observed at temperatures, which are about 40 K higher than the γ^2 -solvus temperatures predicted by ThermoCalc (Fig. 14b–d). In Table 10, the peak temperatures from Figs. 7, 8 and 14 of all four investigated alloys are shown.

In Fig. 15, we compare our ERBO/1 thermal expansion data (presented in red) with results which were published in the literature. The elastic ERBO/1 data we have used so far represent true α_{th} data (red solid line), which were obtained as described in the experimental section of this work. In Fig. 15, we show these data together with mean α_{th} data, which were calculated using 295 K as reference temperature according to:

$$\alpha_{th-MEAN}(T) = \frac{\varepsilon(T) - \varepsilon(295\text{ K})}{T - 295\text{ K}} \quad (6)$$

This is a quantity, which is frequently used in the literature. As can be seen in Fig. 15, the true $\alpha_{th}(T)$ data show the sharp peak, which we exploit for the determination of γ^2 -solvus in the present work, while this feature is largely smoothed out by averaging in the case of $\alpha_{th-MEAN}(T)$. Figure 15 presents digitalized data from different sources [58, 59, 63–71]. All authors performed their experiments using heating rates between 2 K/min and 5 K/min. Data for Ni (full circles) were reproduced from the work of Sung et al. [63], who have created a regression line from various previous data [64–67] and the data for Ni₃Ti (empty circles) were reproduced from the work of Karunaratne et al. [68] (who refer to previous publications [65, 69, 70]). It is interesting to compare these data with dilatometric results for the γ -phase (empty squares) and for the γ^2 -phase data (full squares), which were isolated from CMSX-4 by Siebörger et al. [58]. Their data represent true thermal expansion; however, the isolated phases cannot adjust their chemical composition to γ/γ^2 -equilibrium. Thus, no peak in thermal expansion like that observed in our work appears. Morrow et al. [71] investigated the influence of Mo additions to a Ni-base superalloy with γ/γ^2 -microstructure and showed that increasing Mo levels and Al-levels result in a small decrease in thermal expansion coefficients. In Fig. 15, we reproduce their data for a Ni-based alloy with 3.5% Mo (empty triangles). Finally, we add the recently published CMSX-4 data set from Quedstedt et al. [59] (thick dashed line). The comparison reveals that while there is some scatter, all data are reasonably close when we compare them to our mean thermal expansion coefficient. Note that our mean thermal expansion data and the Quedstedt et al. [59] are in excellent agreement. Our true expansion data, however, deviate significantly toward higher values and show the sharp

peak, which allows to determine the γ^2 -solvus temperature.

Our true thermal expansion data show a pronounced sharp peak (highlighted by an arrow) at high temperatures where the thermal expansion coefficient drops by almost 50%. The data presented in Figs. 7, 8, 9, 13 and 14 clearly suggest that this drop is associated with the γ^2 -solvus temperature. For ERBO/1 (CMSX-4 type), the drop occurs at a temperature, which is very close to the γ^2 -solvus temperature as predicted by ThermoCalc. In case of the three ERBO/15-type alloys, the thermal expansion drop occurs at temperatures, which are 40 K above the predicted γ^2 -solvus temperatures. There is a better agreement between measured (dilatometry) and calculated (ThermoCalc) γ^2 -solvus temperatures for ERBO/1 than for ERBO/15 and its variants (Tables 7 and 8, Figs. 10, 11). This is in line with the finding that the experimentally determined alloy compositions for ERBO/1 (3D-APT, [36], standard material of CMSX-4 type) are in better agreement with the corresponding ThermoCalc predictions than in the case of the experimental ERBO/15 alloys (experimental data: TEM-EDX, [32]). The discrepancy between the γ^2 -solvus temperatures determined experimentally and the ThermoCalc predictions for the ERBO/15 alloys as well as the differences in phase compositions measured in TEM and predicted by ThermoCalc suggest that the ThermoCalc data base needs to be optimized for the new compositional range. The experimental results and the ThermoCalc predictions both suggest that reducing Mo or W levels has no significant effects on the γ^2 -solvus temperatures.

The focus of the present work was on determining γ^2 -solvus temperatures using true thermal expansion measurements. In addition, we report elastic coefficients for four Ni-base single-crystal superalloys, which are useful for engineering design in stress temperature regimes where elasticity governs mechanical material behavior and for estimating thermal stresses associated with thermal fatigue loading. Our results are not directly applicable to assess creep properties. However, γ^2 -solvus temperatures are a measure for the stability of γ^2 -particles, which provide creep strength. Our results is therefore indirectly related to the creep behavior of single-crystal Ni-base superalloys.

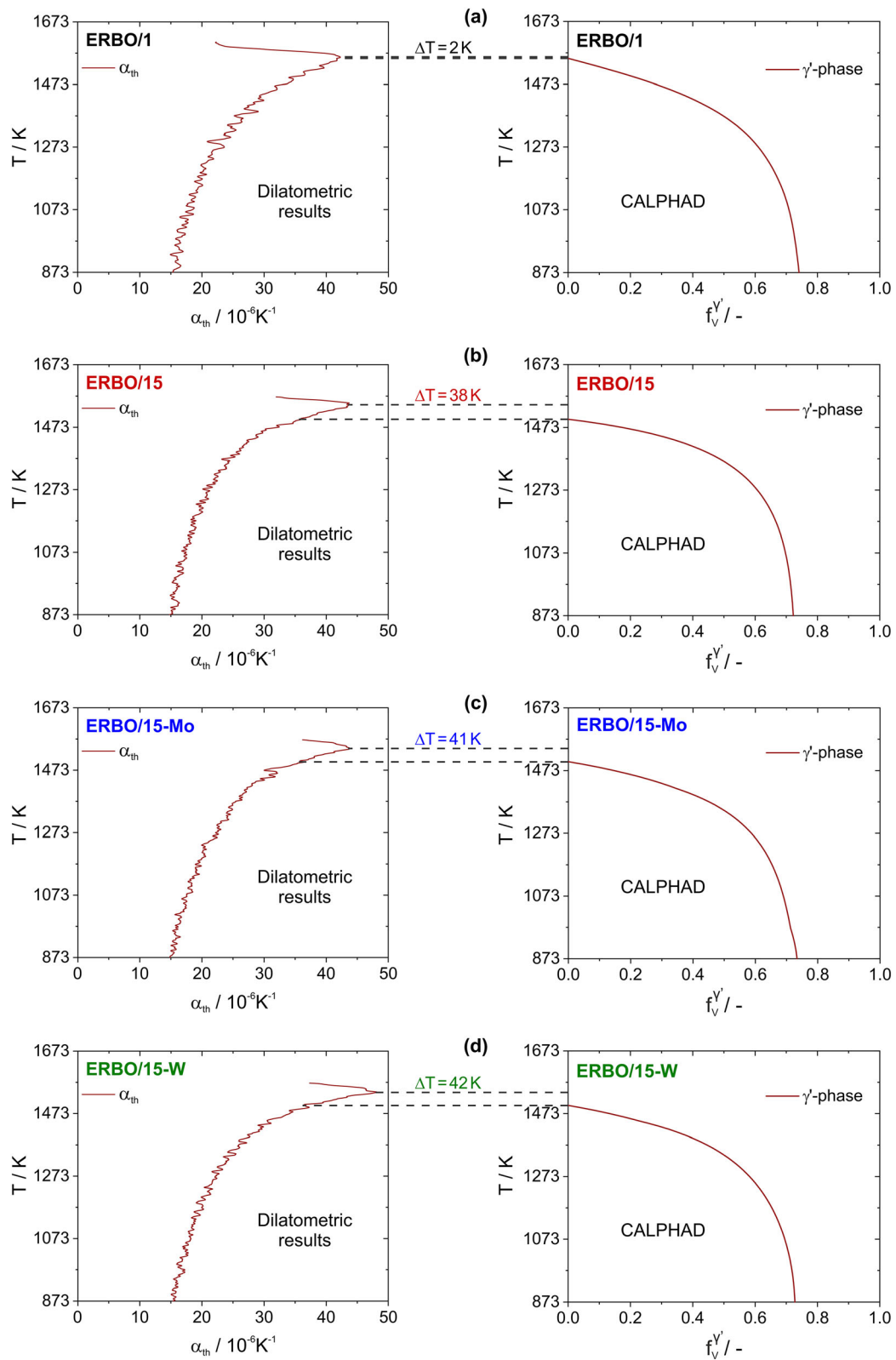


Figure 14 Thermal expansion coefficients (experimental results, left column) and γ^2 -volume fractions (thermodynamic calculations, right column) for the four alloys investigated in the present work. **a** ERBO/1, **b** ERBO/15, **c** ERBO/15-Mo, **d** ERBO/15-W. For details, see text.

Summary and conclusions

The present work investigates the influence of alloy chemistry on elastic properties and on γ^2 -solvus temperatures in Ni-base single-crystal superalloys. Results obtained for a CMSX-4 type of alloy (referred to as ERBO/1 with Re) are compared with three experimental Re-free alloys referred to as ERBO/15, ERBO/15-W (less W than ERBO 15) and ERBO/15-Mo (less Mo than ERBO 15). From the results obtained in the present work, the following conclusions can be drawn:

- (1) The elastic properties of ERBO/15 and its two leaner derivatives do not strongly deviate from the ERBO/1 data, which were recently reported by Demtröder et al. [41]. Fit equations, which describe the temperature dependencies of the elastic moduli $E_{\langle 100 \rangle}$, $E_{\langle 110 \rangle}$ and $E_{\langle 111 \rangle}$ are reported.
- (2) Decreasing W and Mo levels in ERBO/15 result in a small decrease in elastic stiffness (c_{11} , c_{12}). This effect correlates with the electronegativity rather than with the atomic size. It does not strongly affect the values of the macroscopic elastic moduli.
- (3) The thermal expansion behavior of superalloy single crystals does not strongly depend on whether the as-cast or fully heat-treated conditions are considered.
- (4) A comparison between thermodynamic CALPHAD calculations and experimentally observed temperature dependencies of the thermal expansion coefficients suggests that the transition from a low-temperature material state with a high γ^2 -volume fraction to a single-phase γ -material at high temperatures governs the observed behavior.
- (5) A sharp peak in the true thermal expansion coefficient vs. temperature curves indicates the γ^2 -solvus temperature. The experimental peak

positions are in excellent agreement with ThermoCalc predictions for ERBO/1. There is a difference of the order of 40 K in case of ERBO/15 and its two leaner derivatives. This is most probably related to the quality of thermodynamic data available for the new alloy compositions, which can be concluded from the fact that experimental measurements of phase compositions also show some deviation from CALPHAD predictions.

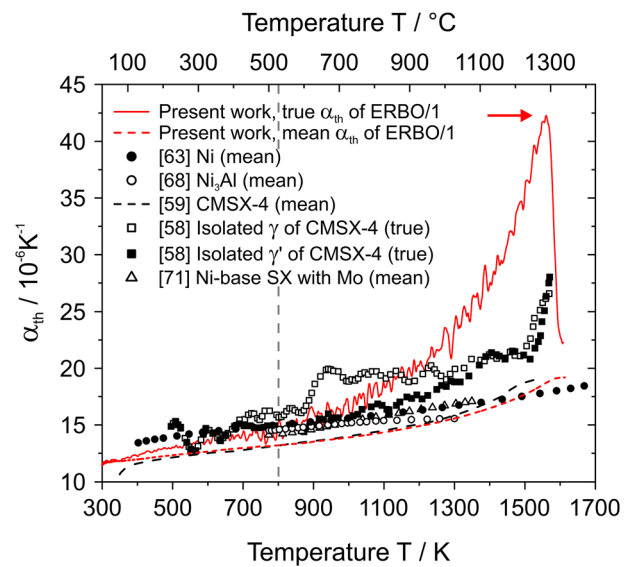


Figure 15 Thermal expansion coefficients vs. temperature data, which were taken from the present work (ERBO/1-C) and literature. Our data are shown in red, true expansion coefficients full red line, mean expansion coefficient dashed red line). Ni (full circles) data were taken from Sung et al. [63]; Ni₃Ti (empty circles) were taken from the work of Karunaratne et al. [68]; CMSX-4 data (dashed black line): Qusted et al. [59]; Isolated γ (empty squares) and isolated γ' (full squares) of CMSX-4 taken from Siebörger et al. [58]; SX with Mo (empty triangles) from Morrow et al. [71].

Table 10 Temperature of maximum thermal expansion measured for the four alloys investigated in the present work. T_{peak} represents the temperature where the sharp maximum occurs in the dilatometric experiments

Alloy	ERBO/1-C	ERBO/15-A	ERBO/15-Mo-A	ERBO/15-W (as-cast)	ERBO/15-W (heat-treated)
$T_{\text{peak}} / \text{K}$	1557	1544	1542	1541	1553
$T_{\text{solvus}} / \text{K}$	1555	1506	1501	1499	1499

T_{solvus} shows the calculated solvus temperature by ThermoCalc.

Acknowledgement

This work was funded by the German research association (Deutsche Forschungsgemeinschaft, DFG) in the framework of the collaborative research center SFB/TR 103. The authors appreciate funding through projects A1 (OMH, EG), B1 (PG, CK) and Z01 (PG, CK). The authors would like to acknowledge fruitful discussions with Dr. Suzana G. Fries (Computational Thermodynamics: CALPHAD, Scientific Guest, Ruhr-University Bochum) and the performance of field emission electron microprobe measurements by Dr. Niels Jöns and Sabine Weisel (Department of Geology, Mineralogy and Geophysics, Ruhr-University Bochum).

Funding

Open Access funding enabled and organized by Projekt DEAL.

Data availability

The raw/processed data required to reproduce these findings cannot be shared at this time as the data also form part of an ongoing study.

Compliance with ethical standards

Conflict of interest The authors declare that they have no known competing financial interests or personal relationships that could have appeared to influence the work reported in this paper. Our work is funded by through the collaborative research center SFB/TR 103 (Fundamentals for a new superalloy technology). We have no direct commercial interest. No experiments involving human tissue were carried out.

Open Access This article is licensed under a Creative Commons Attribution 4.0 International License, which permits use, sharing, adaptation, distribution and reproduction in any medium or format, as long as you give appropriate credit to the original author(s) and the source, provide a link to the Creative Commons licence, and indicate if changes were made. The images or other third party material in this article are included in the article's Creative Commons licence, unless indicated otherwise in a credit line to

the material. If material is not included in the article's Creative Commons licence and your intended use is not permitted by statutory regulation or exceeds the permitted use, you will need to obtain permission directly from the copyright holder. To view a copy of this licence, visit <http://creativecommons.org/licenses/by/4.0/>.

References

- [1] Durand-Charre M (1998) *The Microstructure of superalloys*. Taylor and Francis, Amsterdam
- [2] Pollock TM, Tin S (2006) Nickel-based superalloys for advanced turbine engines: Chemistry, microstructure and properties. *J Propuls Power* 22:361–374
- [3] Reed RC (2008) *The superalloys: fundamentals and applications*. Cambridge University Press, England
- [4] Bürgel R, Maier HJ, Niendorf T (2011) *Handbuch der Hochtemperatur-Werkstofftechnik*. Vieweg Verlag, Wiesbaden
- [5] Völkl R, Glatzel U, Feller-Kniepmeier M (1998) Measurement of lattice misfit in the single crystal nickel based superalloys CMSX-4, SRR 99 and SC 16 by convergent beam electron diffraction. *Acta Mater* 46:4395–4404
- [6] Mughrabi H (2014) The importance of sign and magnitude of γ/γ' lattice misfit in superalloys—with special reference to the new γ' -hardened cobalt-base superalloys. *Acta Mater* 81:21–29
- [7] Pineau A (1976) Influence of uniaxial stress on morphology of coherent precipitates during coarsening – elastic energy considerations. *Acta Met* 24:559–564
- [8] Kuhn HA, Biermann H, Ungar T, Mughrabi H (1991) An X-ray study of creep-deformation induced changes of the lattice mismatch in the γ' hardened monocrystalline nickel-base superalloy SRR-99. *Acta Met Mat* 39:2783–2794
- [9] Pollock TM, Argon A (1992) Creep resistance of CMSX-3 nickel-base superalloy single crystals. *Acta Met Mat* 40:1–30
- [10] Field RD, Pollock TM, Murphy WH (1992) The development of γ/γ' interfacial dislocation networks during creep in Ni-base superalloys. In: *Superalloys 1992*, Antolovich SD et al (eds), TMS, Pennsylvania, pp 557–566
- [11] Socrate S, Parks DM (1993) Numerical determination of the elastic driving force for directional coarsening in Ni-superalloys. *Acta Met Mat* 41:2185–2209
- [12] Keller RR, Maier HJ, Mughrabi H (1993) Characterization of interfacial dislocation networks in a creep-deformed nickel-base superalloy. *Scripta Met Mat* 28:23–28
- [13] Eggeler G, Dlouhy A (1997) On the formation of $\langle 010 \rangle$ -dislocations in the γ' -phase of superalloy single crystals

- during high temperature and low stress creep. *Acta Mater* 45:4251–4262
- [14] Probst-Hein M, Dlouhy A, Eggeler G (1999) Interface dislocations in superalloy single crystals. *Acta Mater* 47:2497–2510
- [15] Matan N, Cox DC, Rae CMF, Reed RC (1999) On the kinetics of rafting in CMSx-4 superalloy single crystals. *Acta Mater* 47:2031–2045
- [16] Nembach E (1997) Particle Strengthening of Metals and Alloys. John Wiley and Sons, New York
- [17] Chandran M, Sondhi SK (2011) First-principle calculation of APB energy in Ni-based binary and ternary alloys. *Modeling Simul Mater Sci Eng* 19:025008–025015
- [18] Vamsi KV, Karthikeyan S (2012) Effect of off-stoichiometry and ternary additions on planar fault energies in Ni3Al. In: *Superalloys 2012*, Huron ES et al (eds). TMS, Pennsylvania, pp 521–530
- [19] Long HB, Liu YN, Kong DL, Wei H, Chen YH, Mao SC (2017) Shearing mechanisms of stacking fault and anti-phase boundary forming dislocation pairs in the γ' -phase of Ni-base superalloys. *J Alloys Compounds* 724:287–295
- [20] Kumar K, Sankarasubramanian R, Waghmare UV (2018) Tuning planar fault energies of Ni3Al with substitutional alloying: First-principles description for guiding rational alloy design. *Scripta Mater* 142:74–78
- [21] Gleiter H, Hornbogen E (1965) Aushärtung durch kohärente geordnete Teilchen. *Acta Metall* 13:576–578
- [22] Vorontsov VA, Shen C, Wang Y, Dye D, Rae CMF (2010) Shearing of γ' -precipitates by $\langle 112 \rangle$ dislocation ribbons in Ni-base superalloys: A phase field approach. *Acta Mater* 58:4110–4119
- [23] Eggeler Y, Titus M, Suzuki A, Pollock T (2014) Creep deformation-induced antiphase boundaries in L₁₂-containing single-crystal cobalt-base superalloys. *Acta Mater* 77:352–359
- [24] Sato A, Moverare JJ, Hasselquist M, Reed RC (2012) On the mechanical behavior of a new single-crystal superalloy for industrial gas turbine applications. *Met Mat Trans A* 43:2302–2315
- [25] Qiu CL, Andrews P (2013) On the formation of irregular-shaped γ' and serrated grain boundaries in a nickel-based superalloy during continuous cooling. *Mat Char* 76:28–34
- [26] Gilles R, Mukherjee D, Eckerlebe H, Karge L, Staron P, Strunz P, Lippmann Th (2014) Investigations of early stage precipitation in a tungsten-rich nickel-base superalloy using SAXS and SANS. *J Alloys Comp* 612:90–97
- [27] Raza SS, Ahmad T, Manzoor MU, Kamran M, Ahmad R (2017) Analysis of metallurgical aspects and their role in processing and performance of superalloys. *J Fundamental Appl Sci* 9:485–498
- [28] Bassini E, Marchese G, Cattano G, Lombardi M, Biamino S, Ugues D, Vallilo G, Picque B (2017) Influence of solutioning on microstructure and hardness of hot isostatically pressed Astroloy. *J Alloys Compounds* 723:1082–1090
- [29] D'Souza N, Li W, Argyrakis C, West GD, Slater CD (2019) On the evolution of primary γ' precipitates during high temperature and high strain rate deformation and subsequent heat treatment in the Ni-based superalloy RR 1000. *Met Mat Trans A* 50:4205–4222
- [30] Pollock TM, Van der Ven A (2019) The evolving landscape for alloy design. *MRS Bull* 44:238–246
- [31] Kumari G, Boehlert C, Sankaran S, Sundaraman M (2020) The effect of solutionizing temperature on the microstructure of Allvac 718 Plus. *J Mat Eng Perf.* <https://doi.org/10.1007/s11665-020-04687>
- [32] Horst OM, Adler D, Git P, Wang H, Streitberger J, Holtkamp M, Jöns N, Singer RF, Körner C, Eggeler G (2020) Exploring the fundamentals of Ni-based superalloy single crystal (SX) alloy design: Chemical composition vs. microstructure. *Mater Des* 195:108976
- [33] Horst OM, Ibrahimkhel S, Streitberger J, Wochmjakow N, Git P, Scholz F, Thome P, Singer RF, Körner C, Frenzel J, Eggeler G (2020) On the influence of alloy composition on creep behavior of Ni-based single-crystal superalloys (SXs). In: *Superalloys 2020*, Tin S et al (eds). TMS, Pennsylvania, pp 60–70
- [34] Rettig R, Matuszewski K, Müller A, Helmer HE, Ritter NC, Singer RF (2016) Development of a low-density rhenium-free single crystal nickel-based superalloy by application of numerical multi-criteria optimization using thermodynamic calculations. In: *Superalloys 2016*, Hardy MC et al (eds). TMS, Pennsylvania, pp 35–44
- [35] Andersson J-O, Helander T, Höglund L, Shi P, Sundman B (2002) THERMO-CALC & DICTRA, Computational tools for materials science. *Calphad* 26:273–312
- [36] Parsa AB, Wollgramm P, Buck H, Somsen C, Kostka A, Povstugar I, Choi P, Raabe D, Dlouhy A, Müller J, Spiecker E, Demtröder K, Schreuer J, Neuking K, Eggeler G (2015) Advanced scale bridging microstructure analysis of single crystal Ni-based superalloys. *Adv Eng Mat* 17:216–230
- [37] Wu X, Wollgramm P, Somsen C, Dlouhy A, Kostka A, Eggeler G (2016) Double minimum creep of single crystal Ni-base superalloys. *Acta Mater* 112:242–260
- [38] Every AG, Sachse W (2001) Handbook of elastic properties of solids, liquids, and gases. Academic Press, London
- [39] Leisure RG, Willis FA (1997) Resonant ultrasound spectroscopy. *J phy condensed matter.* 9(28):6001
- [40] Wollgramm P, Bürger D, Parsa AB, Neuking K, Eggeler G (2016) The effect of stress, temperature and loading direction

- on the creep behaviour of Ni-base single crystal superalloy miniature tensile specimens. *Mater High Temp* 33:346–360
- [41] Demtröder K, Eggeler G, Schreuer J (2015) Influence of microstructure on macroscopic elastic properties and thermal expansion of nickel-base superalloys ERBO/1 and LEK94. *Materialwiss Werkstofftech* 46:563–576
- [42] Swalin RA (1972) *Thermodynamics of solids*. Wiley, New York
- [43] Gaskell DR (2003) *Introduction to the thermodynamics of materials*. Taylor and Francis, New York
- [44] Porter DA, Easterling KE, Sherif MY (2009) *Phase transformations in metals and alloys*. CRC Press, Boca Raton
- [45] Kaufman L, Bernstein H (1970) *Computer calculation of phase diagrams with special reference to refractory metals*. Academic Press Inc, New York
- [46] Lukas HL, Fries SG, Sundman B (2007) *Computational thermodynamics: The calphad method*. Cambridge University Press, Cambridge
- [47] Yardley V, Povstugar I, Choi PP, Raabe D, Parsa AB, Kostka A, Somsen C, Dlouhy A, Neuking K, George EP, Eggeler G (2016) On local phase equilibria and the appearance of nanoparticles in the microstructure of single-crystal Ni-base superalloys. *Adv Eng Mater* 18:1556–1567
- [48] Slater JC (1964) Atomic radii in crystals. *J Chem Phys* 41:3199–3204
- [49] Pauling L (1967) *The chemical bond*. Cornell University Press, New York
- [50] James AM, Lord MP (1992) *Macmillan's chemical and physical data*. Macmillan, London
- [51] Davis JR (1998) *Metals handbook*. ASM International, Ohio
- [52] Schulze GER (1974) *Metallphysik*, 2nd edn. Springer Verlag, Berlin
- [53] Weißmantel C, Hamann C (1979) *Grundlagen der Festkörperphysik*. Springer Verlag, Berlin
- [54] Cahn RW, Siemers PA, Geiger JE, Bardhan P (1987) The order-disorder transformation in Ni₃Al and Ni₃Al-Fe Alloys – I. Determination of the transition temperatures and their relation to ductility. *Acta Met* 35:2737–2751
- [55] Grosdidier T, Hazotte A, Simon A (1998) Precipitation and dissolution process in γ/γ' single crystal nickel-based superalloys. *Mater Sci Eng A* 256:183–196
- [56] Jackson RW, Titus MS, Begley MR, Pollock TM (2016) Thermal expansion behavior of new Co-based alloys and implications for coatings. *Surf & Coat Techn* 289:61–68
- [57] Volz N, Zenk CH, Cherukuri R, Kalfhaus T, Weiser M, Makineni SK, Betzing C, Lenz M, Gault B, Fries SG, Schreuer J, Vassen R, Virtanen S, Raabe D, Spiecker E, Neumeier S, Göken M (2018) Thermophysical and mechanical properties of advanced single crystalline Co-base superalloys. *Met Mat Trans A* 49A:4099–4109
- [58] Siebörger D, Brehm H, Wunderlich F, Möller D, Glatzel U (2001) Temperature dependence of lattice parameter, misfit and thermal expansion coefficient of matrix, γ' phase and superalloy. *Z Metallkde* 92:58–61
- [59] Quedstedt PN, Brooks RF, Chapman L, Morrell R, Youssef Y, Mills KC (2009) Measurement and estimation of thermo-physical properties of nickel based superalloys. *Mater Sci and Techn* 25:154–162
- [60] Simmons RO, Balluffi RW (1960) Measurements of equilibrium vacancy concentrations in aluminum. *Phys Rev* 117:52–61
- [61] Hämäläinen M, Laine E, Tarna T (1969) Thermal expansion of the Ag₃Mg Alloy in the ordered and disordered states. *J Appl Cryst* 2:95–101
- [62] Anraku T, Sakaiharu I, Hoshikawa T, Taniwaki M (2009) Phase transition and thermal expansion behavior in AuCu alloy. *Mat Trans* 50:683–688
- [63] Sung PK, Poirier DR (1998) Estimation of densities and coefficients of thermal expansion of solid Ni-base superalloys. *Mater Sci Eng A* 245:135–141
- [64] Goldsmith TE, Waterman TE, Hirschhorn HJ (1961) *Handbook of Thermophysical Properties of Solid Materials*. Macmillan, New York
- [65] Touloukian YS, Kirby RK, Taylor RE, Desai PD (1975) *Thermophysical properties of matter - the TPRC data series*. Purdue University, Indiana, Thermal expansion metallic elements and alloys
- [66] Drotning WD (1982) Thermal Expansion of Nickel to 2300 K. In: *Thermal Expansion 7*, Larsen DC (ed). Springer, Boston
- [67] Brandes EA, Brook GB (1992) *Smithells Metals Reference Book*. Butterworth-Heinemann, Oxford
- [68] Karunaratne MSA, Kyaw S, Jones A, Morrell R, Thomson RC (2016) Modelling the coefficient of thermal expansion in Ni-based superalloys and bond coatings. *J Mater Sci* 51:4213–4226
- [69] Taylor A, Floyd RW (1953) The constitution of nickel-rich alloys of the nickel-titanium-aluminum system. *J Inst Met* 81:25
- [70] Arbutov MP, Zelenkov IA (1964) Thermal expansion of certain transition metals and alloys on their base. *Phys Met Metallogr* 18:311–312
- [71] Morrow H, Sponseller DL, Semchyshe M (1975) The effects of molybdenum and aluminum on the thermal expansion coefficients of nickel-base alloys. *Met Trans A* 6A:477–485

Publisher's Note Springer Nature remains neutral with regard to jurisdictional claims in published maps and institutional affiliations.